UNIVERSITY OF OKLAHOMA

GRADUATE COLLEGE

CASIMIR ENERGIES OF CAVITIES: THE GEOMETRY QUESTION

A DISSERTATION

SUBMITTED TO THE GRADUATE FACULTY

in partial fullfillment of the requirements for the

Degree of

DOCTOR OF PHILOSOPHY

By

IROKO KOMI ELOM ABALO
Norman, Oklahoma
2012

CASIMIR ENERGIES OF CAVITIES: THE GEOMETRY QUESTION

A DISSERTATION APPROVED FOR THE
HOMER L. DODGE DEPARTMENT OF PHYSICS AND ASTRONOMY

BY

Dr. Kimball Milton, Chair

Dr. Nikola Petrov

Dr. Phillip Gutierrez

Dr. Ronald Kantowski

Dr. Deborah Watson

Acknowledgements

Isaac Newton famously acknowledged "standing on the shoulders of giants." I can hardly refute those words. I am grateful to my advisor Kimball Milton for giving me the opportunity to experience the world of theoretical physics from dizzying heights. It has been an interesting experience, and one from which I have gained a lot. I wish to thank Lev Kaplan whose contributions in our articles have encouraged my continued explorations in uncharted territories. I am also grateful for the many lessons I have learned through my interactions with Kesheng Yang, Andre Lessa, and my fellow research group members (at various stages of my graduate student career): Jef Wagner, Prachi Parashar, Nima Pourtolami. Their support in many ways such as helping with my naive questions or simply upgrading my bipedal mode of transportation to an automotive locomotion in times of necessity has been crucial. Thank you. Finally, I want to thank my family for their constant support.

Table of Contents

List of Tables

List of Figures

Abstract

The question of how the Casimir effect relates to a system's geometry is of fundamental interest. In this thesis, we present new results for interior Casimir self-energies of various integrable geometries and show interesting systematic relations between these energies. In particular, we consider prisms with triangular cross sections (equilateral, hemiequilateral, and right isosceles triangles), triangular polygons of the same cross sections, and three tetrahedra. The triangular prisms are of infinite or finite lengths. We obtain interior Casimir energies for these cavities subject to Dirichlet and Neumann boundary conditions. In addition to these boundary conditions, we also obtain electromagnetic Casimir energies for the infinite prisms.

These energies are regularized using various consistent methods, one of which is regularization by point-splitting. Summing these modes explicitly using a cylinder kernel formulation, we show that the correct Weyl divergences are obtained. We also give closed-form results for the infinite triangular prisms. In order to understand the geometry dependence of these energies, we rederive well-known results for rectangular parallelepipeds (including the cube) and infinite rectangular prisms.

The analysis of these self-energies yields intriguing results. By plotting the scaled energies against the appropriately chosen isoperimetric or isoareal quotients, we observe interesting patterns, which hint towards a systematic functional dependence. In addition to the calculation of new Casimir energies, this constitutes a significant contribution to the theoretical understanding of self-energies and has interesting implications.

Chapter 1

Introduction

1.1 Historical Background

In 1953, when H. B. G. Casimir proposed his model of the electron [1], few would have convincingly thought otherwise. After all, in 1948, Casimir had shown the world that energy differences in the vacuum due to the imposition of two parallel conducting plates resulted, in theory, in a net attractive force between the plates [2]. He predicted that two infinite perfectly conducting plates separated by a distance a would experience an energy per area,

$$\mathcal{E} = -\frac{\pi^2 \hbar c}{720\, a^3}\,, \tag{1.1}$$

which implies a force per area on the plates:

$$\mathcal{F} = -\frac{d}{da}\mathcal{E} = -\frac{\pi^2 \hbar c}{240\, a^4}\,. \tag{1.2}$$

The first attempt to measure this force, on the order of $-1.30 \times 10^{-27}\,\mathrm{N\,m^2\,a^{-4}}$ [3], was an inconclusive experiment in 1958 by Sparnaay [4]. More conclusive measurements followed towards the end of the 20th century [5–8]. However, in 1953, Casimir's previous attractive result for two parallel plates pointed overwhelmingly to a model of the electron where a similar attractive force due to bounded quantum fluctuations or zero-point energy would offset a repulsive force due to the innate negative charge distribution of the electron. This was not the first of such hypotheses, in fact, it followed in the tradition of the Abraham-Lorentz and Poincaré models for the electron.

Casimir hypothesized that if the electron were considered as a perfectly conducting shell of radius R, a change in the zero-point energy of the system due to quantum vacuum fluctuations would be observed of the form,

$$C\,\frac{\hbar c}{R}\,, \tag{1.3}$$

with $C = e^2/(2\hbar c)$, obtained by a comparison with the electrostatic self-energy. The hypothesis seemed plausible, yet a theoretical verification, at the very least, was still in order. As expected, the verification arrived, almost fifteen years later, in the arduous thesis work of T. H. Boyer [9]. To Boyer's and most of the now-termed *Casimir Effect* community's astonishment, the calculated self-energy of a perfectly conducting spherical shell,

$$E \backsimeq +0.09\,\frac{\hbar c}{2R}\,, \tag{1.4}$$

was of the opposite sign, a repulsive force! This result was verified on numerous occasions using various methods and even improved upon [10–15],

$$E = +0.092353\,\frac{\hbar c}{2R}\,. \tag{1.5}$$

The fact that the electromagnetic self-energy of a conducting spherical shell is repulsive is now accepted knowledge, but such an unexpected dénouement stirred further questions. One, in particular, concerned the link between a system's geometry and its self-energy, since Boyer's result showed a non-intuitive dependence. To this end, numerous calculations have been performed over the years for different geometries: parallelepipeds, cubes, hypercubes, cylinders,..., with no conclusive verdict [16–20].

1.2 Outline

The work presented in this thesis follows in this same vein, but with new and intriguing results [21–23]. In particular, this work showcases new interior Casimir self-energy results for various integrable cavities: triangular prisms, triangular polygons, and tetrahedra. Although, these are new results and deserve attention, the real highlights of this work are the intriguing systematic dependences observed between the geometries' self-energies and their aptly chosen geometric invariants. These systematics are observed for well-known results as well as the newer ones being presented.

We will start with an introduction to the evaluation of Casimir energies by direct mode summation, emphasizing in particular the approach utilizing Green's function. Next, will be a review of the regularization methods which are used for calculations, followed by a section on integrable domains. The last sections will focus on the new Casimir energy results for triangular prisms, and tetrahedra, and an overall analysis and conclusion. Unless explictly given, most of the results in this work will be in natural units, where $\hbar = 1 = c$. We will adopt the convention of assigning the symbol E to Casimir energies of closed cavities and $\mathcal{E}$ to Casimir energies per length or area. A likely source of confusion, prisms will sometimes be referred to as *cylinders* with a cross-sectional distinction. For instance, an infinite equilateral triangular cylinder would denote a prism of equilateral triangular cross section and infinite length. The term *waveguide* will refer to prisms or polygonal cylinders of infinite length.

Chapter 2

Casimir Energy: Mode Summation

2.1 Introduction

The Casimir or vacuum energy of a system is the regularized sum of its modal energies. There are various ways of performing such calculations, yet the most direct method remains the explicit summation over the eigenvalues of the system. As a rough explanation, the quantum mechanical energy of a harmonic oscillator is, $E_n = (n + 1/2)\hbar\omega$, which implies a residual "vacuum" energy when $n = 0$, a particular feature of quantum mechanics (the actual relevant theory is quantum field theory). Therefore, the sum of these residual energies is simply,

$$E = \sum_n \left(\frac{1}{2} \hbar \omega_n \right) . \tag{2.1}$$

Of course, this is only possible if the eigenvalues are known explicitly, which is the case for integrable domains. One would also need to regularize Eq. (2.1), which is formally divergent, with an ad-hoc method such as a regulator function or zeta function regularization. When the eigenvalues are known implicitly, similar methods such as the Argument Principle are useful. The classic example for a direct mode summation is the parallel conducting plate system, Casimir's original 1948 calculation [2]. Casimir starts with Eq. (2.1) for the energy per unit area, which he then writes out explicitly,

$$\mathcal{E} = \frac{\hbar c}{2\pi^2} \int_0^\infty dk_x \, dk_y \sum_{n=-\infty}^{\infty} \sqrt{(n\pi/a)^2 + k_x^2 + k_y^2} \, , \tag{2.2}$$

where a is the plate separation distance. Switching to polar coordinates, $dk_x dk_y \to k\, dk d\theta$, the previous expression becomes,

$$\mathcal{E} = \frac{\hbar c}{\pi} \int_0^\infty k\, dk \sum_{n=-\infty}^{\infty} \sqrt{(n\pi/a)^2 + k^2}\,, \tag{2.3}$$

after the integral on θ. Casimir then subtracts the limit of this expression when $a \to \infty$ to obtain the change in the energy of the system due to the two parallel conducting plates being in place,

$$\Delta\mathcal{E} = \frac{\hbar c}{2\pi}\left(\frac{1}{2}\int_0^\infty k\, dk \sum_{n=-\infty}^{\infty} \sqrt{(n\pi/a)^2 + k^2} - \frac{a}{\pi}\int_0^\infty x\, dx \int_0^\infty dk_z \sqrt{x^2 + k_z^2}\right). \tag{2.4}$$

This previous expression still appears to be divergent, so the author introduces a regulator $f(k/k_m)$, where k_m is a physically motivated cutoff frequency. The idea is that modes of higher frequency are barely contained by the conducting boundaries and therefore contribute less to the energy. The regulator, f, is chosen such that $f(k/k_m) \to 0$ as $k \to \infty$ and $f(k/k_m) = 1$ for $k << k_m$. Finally, after a successive change of variables, Eq. (2.4) can be written in the form,

$$\Delta\mathcal{E} = \frac{\hbar c \pi^2}{4a^3}\left(\frac{1}{2}\sum_{n=-\infty}^{\infty} F(n) - \int_0^\infty dn\, F(n)\right), \tag{2.5}$$

in terms of,

$$F(n) = \int_{n^2}^\infty d\kappa \sqrt{\kappa}\, f\left(\kappa\pi/a k_m\right)\,. \tag{2.6}$$

He, then, makes use of the Euler-Maclaurin formula for an even function, $F(-n) = F(n)$, to obtain:

$$\sum_{n=0}^{\infty} F(n) - \frac{1}{2}F(0) - \int_0^\infty F(n) dn = -\frac{1}{12}F'(0) + \frac{1}{720}F^{(3)}(0) + \dots\,, \tag{2.7}$$

and obtains a single physical contribution from the third-derivative term (the other higher terms are ignored because they contain powers of $\pi a/k_m$, and the result should be independent of k_m),

$$\Delta\mathcal{E} = -\frac{\pi^2\hbar c}{720\,a^3}\,, \tag{2.8}$$

which yields, indeed, an attractive force (See Eq. (1.2)),

$$\mathcal{F} = -\frac{\pi^2\hbar c}{240\,a^4}\,. \tag{2.9}$$

2.2 Green's Function Approach

A roundabout way of summing modal energies directly is the method of Green's function, which has the advantage of automatically generating a regularization method instead of using an ad-hoc method. For the sake of simplicity, we consider a scalar field satisfying Dirichlet or Neumann boundary conditions. The quantum vacuum expectation value of the field's energy density at a point, $x = (\mathbf{r}, t)$, in space-time is given by [3],

$$\langle t^{00}(x)\rangle = \lim_{x\to x'} \frac{1}{i}\,\partial_t\partial_t' G(x,x')\,, \tag{2.10}$$

where $G(x,x')$ is Green's function satisfying the differential equation,

$$\left(\partial_t^2 - \nabla^2\right) G(x,x') = \delta(x-x')\,, \tag{2.11}$$

and the appropriate system boundary conditions. We begin by taking the Fourier transform of time,

$$G(x,x') = \int_{-\infty}^{\infty} \frac{d\omega}{2\pi} e^{-i\omega(t-t')} g(\mathbf{r},\mathbf{r}';\omega). \tag{2.12}$$

The goal, now, is to solve for Green's reduced function $g(\mathbf{r}, \mathbf{r}'; \omega)$. First, we observe that the eigenfunctions of the Laplacian,

$$-\nabla^2 \phi_{\mathbf{m}}(\mathbf{r}) = \lambda_{\mathbf{m}}^2 \phi_{\mathbf{m}}(\mathbf{r}) \,, \tag{2.13}$$

form a complete set:

$$\sum_{\mathbf{m}} \phi_{\mathbf{m}}(\mathbf{r}) \phi_{\mathbf{m}}^*(\mathbf{r}') = \delta(\mathbf{r} - \mathbf{r}') \,. \tag{2.14}$$

After substituting Eq. (2.12) in Eq. (2.11), one notices that Green's reduced function can be defined as,

$$g(\mathbf{r}, \mathbf{r}'; \omega) = \sum_{\mathbf{m}} \frac{\phi_{\mathbf{m}}(\mathbf{r}) \phi_{\mathbf{m}}^*(\mathbf{r}')}{\lambda_{\mathbf{m}}^2 - \omega^2} \,. \tag{2.15}$$

After applying a Euclidean rotation, $\omega \to i\zeta$ and $(t - t') \to i\tau$, the energy density is then written in the form,

$$\langle t^{00}(\mathbf{r}) \rangle = \lim_{\tau \to 0} \sum_{\mathbf{m}} \phi_{\mathbf{m}}(\mathbf{r}) \phi_{\mathbf{m}}^*(\mathbf{r}) \int_{-\infty}^{\infty} \frac{d\zeta}{2\pi} \frac{(-\zeta^2)\, e^{i\zeta\tau}}{\lambda_{\mathbf{m}}^2 + \zeta^2} \,. \tag{2.16}$$

We are now free to perform the integral as a contour integral to obtain,

$$\langle t^{00}(\mathbf{r}) \rangle = \frac{1}{2} \lim_{\tau \to 0} \sum_{\mathbf{m}} \phi_{\mathbf{m}}(\mathbf{r}) \phi_{\mathbf{m}}^*(\mathbf{r}) \sqrt{\lambda_{\mathbf{m}}^2}\, e^{-|\tau| \sqrt{\lambda_{\mathbf{m}}^2}} \,. \tag{2.17}$$

To obtain the energy, we simply integrate the energy density over the system's volume while choosing $\tau > 0$,

$$\langle T^{00} \rangle = E = \frac{1}{2} \lim_{\tau \to 0} \sum_{\mathbf{m}} \sqrt{\lambda_{\mathbf{m}}^2}\, e^{-\tau \sqrt{\lambda_{\mathbf{m}}^2}} \,. \tag{2.18}$$

Again, we have used the orthonormality relation of Laplacian eigenfunctions,

$$\int_V d\mathbf{r}\, \phi_{\mathbf{m}}(\mathbf{r}) \phi_{\mathbf{m}}^*(\mathbf{r}) = 1 \,. \tag{2.19}$$

This approach gives a consistent and automatically point-split regulated expression of the divergent expression in Eq. (2.1) in terms of a traced cylinder kernel [24],

$$E = \frac{1}{2} \lim_{\tau \to 0} \left(-\frac{d}{d\tau} \right) \sum_{\mathbf{m}} e^{-\tau \sqrt{\lambda_{\mathbf{m}}^2}} \,. \tag{2.20}$$

For a cylinder or infinite prism, the energy per unit length is slightly different from the previous expression with an integral over the continuous mode number,

$$\mathcal{E} = \frac{1}{2} \lim_{\tau \to 0} \left(-\frac{d}{d\tau} \right) \int_{-\infty}^{\infty} \frac{dk}{2\pi} \sum_{\mathbf{m}} e^{-\tau \sqrt{k^2 + \lambda_{\mathbf{m}}^2}} \,. \tag{2.21}$$

However, these expressions (Eqs. (2.20) and (2.21)), in their current forms, are meaningless because they contain divergences as $\tau \to 0$. We must remove the divergences in order to obtain a physical result, the change in the vacuum energy of the system.

Chapter 3

Regularization Methods

3.1 Point-Splitting Regularization

The regularization method of choice in this work is the point-splitting method. It flows directly and consistently from the formalism of Green's function. In addition, it allows one to unambiguously identify the divergent pieces, the Weyl terms, while giving the finite parts, the Casimir energies, which can be expressed as sums of Epstein zeta functions. A typical point-split expression for a three-dimensional closed integrable cavity with eigenvalues $\lambda_{\mathbf{m}}^2$ is Eq. (2.20):

$$E = \frac{1}{2} \lim_{\tau \to 0} \left(-\frac{d}{d\tau} \right) \sum_{\mathbf{m}} e^{-\tau \sqrt{\lambda_{\mathbf{m}}^2}} \, . \tag{3.1}$$

The mode numbers, $\mathbf{m} = (k, m, n)$, are constrained to specific ranges depending on the type of boundary condition considered. These constrained ranges may be reformulated in terms of equivalent expressions with unconstrained ranges through a process of addition and subtraction of terms while keeping track of degeneracies. It is then possible to resum such expressions using Poisson's summation formula,

$$\sum_{m=-\infty}^{\infty} f(m) = \sum_{n=-\infty}^{\infty} \left(\int_{-\infty}^{\infty} e^{2\pi i m n} f(m) \, dm \right) , \tag{3.2}$$

basically a Fourier transform, to separate parts that diverge as $\tau \to 0$ from other finite parts. Given a traced cylinder kernel of an arbitrary real quadratic form,

$$\mathcal{S} = \sum_{m_1, \ldots, m_n = -\infty}^{\infty} e^{-\tau \sqrt{(m+a)_j \, A_{jk} \, (m+a)_k}} \, , \tag{3.3}$$

we obtain after following the procedure outlined above (see Appendix A),

$$\mathcal{S} = \frac{2^n \pi^{(n-1)/2}\,\Gamma((n+1)/2)}{|\det(A)|^{1/2}} \sum_{m_1,\ldots,m_n=-\infty}^{\infty} \frac{\tau\, e^{-2\pi i\, m_j\, a_j}}{(\tau^2 + 4\pi^2 k_j\, k_j)^{(n+1)/2}}, \tag{3.4}$$

where one can now clearly identify finite and divergent terms as $\tau \to 0$. The above formula allows us, for instance, to give useful formulæ in regularizing divergent expressions for three-dimensional cavities,

$$\begin{aligned}\Big(-\frac{d}{d\tau}\Big) \sum_{p,q,r=-\infty}^{\infty} e^{-\tau\sqrt{\alpha(p+a)^2+\beta(q+b)^2+\gamma(r+c)^2}} \\ = \frac{24\pi}{\sqrt{\alpha\beta\gamma}\,\tau^4} - \frac{1}{2\pi^3\sqrt{\alpha\beta\gamma}} \sum_{p,q,r=-\infty}^{\infty}{}' \frac{e^{-2\pi i(pa+qb+rc)}}{(p^2/\alpha + q^2/\beta + r^2/\gamma)^2}\,,\end{aligned} \tag{3.5}$$

$$\begin{aligned}\Big(-\frac{d}{d\tau}\Big) \sum_{p,q=-\infty}^{\infty} e^{-\tau\sqrt{\alpha(p+a)^2+\beta(q+b)^2}} \\ = \frac{4\pi}{\sqrt{\alpha\beta}\,\tau^3} - \frac{1}{4\pi^2\sqrt{\alpha\beta}} \sum_{p,q=-\infty}^{\infty}{}' \frac{e^{-2\pi i(pa+qb)}}{(p^2/\alpha + q^2/\beta)^{3/2}}\,,\end{aligned} \tag{3.6}$$

$$\Big(-\frac{d}{d\tau}\Big) \sum_{p=-\infty}^{\infty} e^{-\tau\sqrt{\alpha(p+a)^2}} = \frac{2}{\sqrt{\alpha}\,\tau^2} - \frac{\sqrt{\alpha}}{2\pi^2} \sum_{p=-\infty}^{\infty}{}' \frac{e^{-2\pi i(pa)}}{p^2}\,. \tag{3.7}$$

The prime, here, means that all positive and negative integers are included in the sum, but not the case where all the integers are zero.

If a few or all of the mode numbers were continuous (one mode number in the case of infinite cylinders), then the results would be similar except for some subtle changes (see Appendix A). For example, Eqs. (3.5), (3.6), and (3.7) would be slightly modified:

$$\begin{aligned}\Big(-\frac{d}{d\tau}\Big) \int_{-\infty}^{\infty} dp \sum_{q,r=-\infty}^{\infty} e^{-\tau\sqrt{\alpha(p+a)^2+\beta(q+b)^2+\gamma(r+c)^2}} \\ = \frac{24\pi}{\sqrt{\alpha\beta\gamma}\,\tau^4} - \frac{1}{2\pi^3\sqrt{\alpha\beta\gamma}} \sum_{q,r=-\infty}^{\infty}{}' \frac{e^{-2\pi i(qb+rc)}}{(q^2/\beta + r^2/\gamma)^2}\,,\end{aligned} \tag{3.8}$$

$$\Big(-\frac{d}{d\tau}\Big)\int_{-\infty}^{\infty}dp\sum_{q=-\infty}^{\infty}e^{-\tau\sqrt{\alpha(p+a)^2+\beta(q+b)^2}} \tag{3.9}$$

$$=\frac{4\pi}{\sqrt{\alpha\beta}\,\tau^3}-\frac{1}{4\pi^2\sqrt{\alpha\beta}}\sum_{q=-\infty}^{\infty}{}'\,\frac{e^{-2\pi i(qb)}}{(q^2/\beta)^{3/2}}\,,$$

$$\Big(-\frac{d}{d\tau}\Big)\int_{-\infty}^{\infty}dp\;e^{-\tau\sqrt{\alpha(p+a)^2}}=\frac{2}{\sqrt{\alpha}\,\tau^2}\,. \tag{3.10}$$

3.1.1 Weyl Terms

The divergent parts one obtains after regularizing the energy are known as *Weyl terms*. Weyl's work on the asymptotic distribution of eigenvalues showed that, asymptotically, the number of eigenvalues of the Laplacian for a cavity or membrane is related to the geometrical properties of the cavity such as the volume, surface area, etc. [25–28]. This result is known commonly as *Weyl's law*. Also an outcome of Weyl's law, we note that the divergent parts of a regularized cylinder kernel for a cavity or membrane are related to its geometrical attributes. For a closed integrable cavity with Dirichlet (D) or Neumann (N) boundary conditions, the divergent parts are of the form,

$$E_{\rm div}^{(D,N)}=\frac{3V}{2\pi^2\tau^4}\mp\frac{S}{8\pi\tau^3}+\frac{C}{48\pi\tau^2}, \tag{3.11}$$

where the $-/+$ sign is associated respectively with Dirichlet/Neumann boundary conditions and the *corner* term is defined as [29],

$$C=\sum_j\left(\frac{\pi}{\alpha_j}-\frac{\alpha_j}{\pi}\right)L_j\,, \tag{3.12}$$

with α_j and L_j designating respectively the dihedral angles and their corresponding edge lengths. For an infinite prism or polygonal cylinder, the Dirichlet and Neumann

divergent parts are similarly proportional to the area, perimeter, and a corner term,

$$\mathcal{E}_{\text{div}}^{(D,N)} = \frac{3A}{2\pi^2\tau^4} \mp \frac{P}{8\pi\tau^3} + \frac{C}{48\pi\tau^2}. \tag{3.13}$$

The new corner term is defined differently from Eq. (3.12),

$$C = \sum_i \left(\frac{\pi}{\alpha_i} - \frac{\alpha_i}{\pi} \right). \tag{3.14}$$

Only the dihedral angles α_j are needed. This is to be expected, since one cannot define an edge length for an infinite prism. The electromagnetic case for infinite prisms is also feasible. Since it is known that the electromagnetic modes for a cylindrical waveguide of arbitrary cross section separate into two types: one satisfying Dirichlet boundary conditions and the other Neumann boundary conditions [30], we can show that the electromagnetic energies and Weyl terms are simply the sum of their Dirichlet and Neumann counterparts,

$$\mathcal{E}_{\text{div}}^{(EM)} = \frac{3A}{\pi^2\tau^4} + \frac{C}{24\pi\tau^2}. \tag{3.15}$$

Of course, the electromagnetic corner term C is defined identically in Eq. (3.14).

3.2 Dimensional Regularization

Another method of regularization is that of dimensional regularization where one assumes an arbitrary number of dimensions, say d, which is then analytically continued to the correct limit at the end of the calculation. This approach is particularly suited for calculations geared towards dimensionally-related results. For instance, it is convenient when calculating energies of infinite cylinders and their planar polygonal

analogues, which we will demonstrate later in this work. However, compared to the previous method of regularization via point-splitting, this approach fails to give the divergent parts. We start with the Casimir energy per length, $\mathcal{E}$, for infinite cylindrical geometries, generally expressed as a sum over mode frequencies in the following form,

$$\mathcal{E} = \frac{1}{2}\int_{-\infty}^{\infty}\frac{dk}{2\pi}\sum_{\mathbf{m}}\sqrt{k^2+\lambda_{\mathbf{m}}^2}\,, \tag{3.16}$$

where $\lambda_{\mathbf{m}}^2$ are the eigenvalues of the two-dimensional Laplacian,

$$\left(\nabla_\perp^2+\lambda_{\mathbf{m}}^2\right)\Phi_{\mathbf{m}}(\mathbf{r}_\perp)=0\,, \tag{3.17}$$

$\mathbf{m}=(m,n)$ is a pair of mode numbers satisfying completeness constraints, and $\Phi_{\mathbf{m}}(\mathbf{r}_\perp)$ satisfies the given boundary conditions on the cylinder's surface. Here, $\mathbf{r}_\perp$ denotes the two coordinates transverse to the longitudinal cylinder axis. One proceeds by extending the one dimension for the longitudinal wavevector k to d dimensions, $dk\to d^dk$. Is then possible after a few manipulations to write Eq. (3.16) in the form,

$$\mathcal{E} = -\lim_{d\to 1}\frac{\Gamma(-(1+d)/2)}{2^{d+2}\pi^{(d+1)/2}}\sum_{\mathbf{m}}\left(\lambda_{\mathbf{m}}^2\right)^{(1+d)/2}. \tag{3.18}$$

One notes that in the limit $d\to 1$, we obtain a $\Gamma(-1)$ divergence. However, one can surmount this problem by analytic continuation. For the cylindrical and polygonal geometries considered, which have two-dimensional cross sections, the eigenvalue expression $\lambda_{\mathbf{m}}^2$ is a simple quadratic form in m and n. This allows us to employ the Chowla-Selberg formula, an exact formula for a class of Epstein zeta functions [31,32], given in Appendix B, and thereby utilize the reflection property of the zeta function,

$$\Gamma(s)\zeta(2s)\pi^{-s}=\Gamma\left(\frac{1-2s}{2}\right)\zeta(1-2s)\pi^{-(1-2s)/2}\,, \tag{3.19}$$

which allows us to analytically continue $d\to 1$.

3.3 Closed-Form Zeta Regularization

For the particular cases of square, and right isosceles, equilateral, and hemiequilateral triangular cross sections, it is possible to write the finite results in a closed-form. This rather impressive possibility is due to the fact that certain Epstein zeta functions may be written as products of other elementary functions [33–39]. While it is feasible to obtain such closed-form results for integrable polygons and polygonal cylinders, it is not the case, at least currently, for integrable polyhedral cavities.

Chapter 4

Reflective Cavities

4.1 The Method of Images

A classic problem in electrostatics is finding the electric potential for a point charge in front of an infinite grounded plate. It is often surprising to note that such a problem has the same solution as that of two opposite point charges placed at equal distances along a perpendicular to a hypothetical infinite plane. The second configuration satisfies the boundary conditions of the first, and given the uniqueness of the solution, one has indeed solved the problem. Note, however, that since we have essentially solved the problem by introducing an image charge perpendicularly opposite to the original charge, the solution is only valid in the region containing the original charge. This is the well-known *method of images*.

One may wonder whether other situations may lend themselves to such a quirky solution, and if so how many. Indeed, there are other cases that have been described in various articles and books [30, 40–43]; in particular, we will limit ourselves to polygonal and polyhedral cases. There are, possibly, various methods to identify these cavities. The one we outline in the following sections is mostly from Ref. [40].

4.1.1 Polygons

The key to being able to consistently introduce a set of image charges without any overlapping is having the appropriate angles. By imagining a point charge wedged

between two semi-infinite planes intersecting at an angle α, one observes that in order to accommodate an even number of point charges one needs α to be an even fraction of 2π, which implies $\alpha = \pi/n$, where n is a positive integer. This allows us to enumerate all the possible wedge angles: π (an infinite plate), $\pi/2$, $\pi/3\ldots$. Armed with this knowledge, one can then construct polygons with these particular angles and therefore guarantee the use of the image method. The sum of the angles for an n-sided polygon is $(n-2)\pi$, which when combined with the constraints on the choice of angles gives four cases [40]:

- Right isosceles triangles $(\pi/2|\pi/4|\pi/4)$
- Equilateral triangles $(\pi/3|\pi/3|\pi/3)$
- Hemiequilateral triangles $(\pi/2|\pi/3|\pi/6)$
- Rectangles $(\pi/2|\pi/2|\pi/2|\pi/2)$

It appears there are few treatments of Casimir energy calculations for polygonal domains. One reason may be that such geometries are less physically motivated. Two prominent articles are Refs. [19, 44]. The first reference considers the square geometry when computing zero-point energies for hypercubes; the second reference gives the self-energy for an equilateral geometry with Dirichlet boundary conditions. In this work we will give new self-energies for the last two triangles: right isosceles and hemiequilateral triangles. These results are for Dirichlet and Neumann boundary conditions.

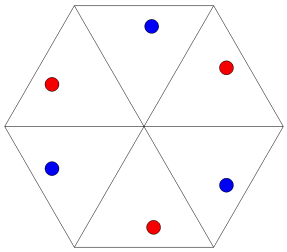

Figure 4.1: Primitive cell for an equilateral triangle. This is obtained by repeated reflections across the triangle's boundaries meeting at the origin. With repeated translations along primitive lattice vectors, this cell tiles the plane. For an electrostatic problem, the red and blue circles would represent positive and negative charges.

4.1.2 Polyhedrons

Similar conditions apply for reflective polyhedrons. By analogy, we should seek to construct these polyhedrons with special corners which allow a consistent set of reflected images. First, one considers a point charge wedged in a corner resulting from the intersection of n planes and starts by enforcing the dihedral angles of the corner to be of the form π/m, where m is again a positive integer. Since the sum of the interior dihedral angles α_j must satisfy the inequalities,

$$(n-2)\pi < \sum_j \alpha_j < (n+2)\pi\,, \tag{4.1}$$

the allowed corners are all found to be trihedral corners [40]:

- $(\pi/2|\pi/2|\pi/n)$, where n is a positive integer
- $(\pi/2|\pi/3|\pi/3)$

- $(\pi/2|\pi/3|\pi/4)$
- $(\pi/2|\pi/3|\pi/5)$

Such corners are known as Möbius corners. Again, building polyhedrons out of these trihedral corners yields a finite number of cases [40, 42]:

- Three tetrahedra
- Three triangular prisms
- Rectangular prisms

The prisms can be of finite or infinite length. Casimir energy calculations for rectangular prisms can be found in many articles [16–19]; however, almost no attention has been paid to the integrable tetrahedra and triangular prisms. Moreover, the only treatments of such cavities, Refs. [45–47] appear to be erroneous. In the coming sections, we will present new and correct treatments of these cavities. First, we will address the construction of eigenfunctions and eigenvalues for reflective domains.

4.2 Eigenmodes

The cavities listed in the previous sections are all soluble using the method of images. The approach we describe below is found in Terras and Swanson's elegant work [40, 41, 48], in particular Ref. [48]. The authors find that solutions for reflective domains are best expressed in the language of group theory. They first start with a few preliminary definitions.

Let E_n be the space of real cartesian vectors of the form $(x_1, x_2, \ldots, x_n)$. For our work we will consider $n = 2$ or 3. Let V denote a domain or cavity in E_n with boundaries defined by linear equations, in other words lines or planes depending on the dimension. Let G be the space group associated with the domain V. In order for V to be an image domain, i.e. an integrable cavity, the set $\{g \cdot x | g \in G\}$ must have one and only one element in V. If there were to be more than one element in V, then it would be impossible to apply the image method, and V would not be an image domain.

The space group G is defined in terms of (S, L), where S is the point group generated by reflections across the domain's boundaries, and L is the corresponding primitive lattice. The symmetries of the space group consist of the combination of the point group operations σ (reflections, rotations, etc.) and translations by lattice vectors $\mathbf{n}$, which are succinctly defined as

$$(\sigma, \mathbf{n})\mathbf{r} = \sigma \cdot \mathbf{r} + \mathbf{n}\,. \tag{4.2}$$

The set of dual lattice vectors L' is chosen such that the inner product between a primitive lattice vector and a dual lattice vector is an integer number,

$$L' = \{\mathbf{m} \in E_n | \langle \mathbf{m} | \mathbf{n} \rangle \in \mathbb{Z}, \forall \mathbf{n} \in L\}\,. \tag{4.3}$$

4.2.1 Dirichlet BC

The Dirichlet eigenfunction for an image domain V is then written in a very convenient form,

$$\Phi_{\mathbf{m}}(\mathbf{r}) = \sum_j \det(\sigma_j)\, e^{2\pi i \langle \mathbf{m}|\sigma_j|\mathbf{r}\rangle}\,, \tag{4.4}$$

where, $j = 1, 2, \ldots$, is an index of the elements σ_j of the point group S, and $\mathbf{m}$ is a dual lattice vector. In this form, it is straightforward to check that $\Phi_{\mathbf{m}}(\mathbf{r})$ does indeed satisfy Dirichlet boundary conditions. Using group properties and the previous definitions, they observe that,

$$\Phi_{\mathbf{m}}((\sigma_b, \mathbf{n})\mathbf{r}) = \det(\sigma_b)\Phi_{\mathbf{m}}(\mathbf{r}) = \Phi_{\sigma_b \cdot \mathbf{m}}(\mathbf{r})\,. \tag{4.5}$$

With σ_b, a reflection operator corresponding to one of the domain's boundaries, one sees that when $\mathbf{r}$ or $\mathbf{m}$ is chosen to lie on the said boundary, $\Phi_{\mathbf{m}}(\mathbf{r})$ is null. This not only shows that Eq. (4.4) satisfies Dirichlet boundary conditions, but also gives the conditions on the mode numbers which make the eigenfunctions unphysical.

4.2.2 Neumann BC

Similary, with the usual definitions, the Neumann mode is written as,

$$\Psi_{\mathbf{m}}(\mathbf{r}) = \sum_j e^{2\pi i \langle \mathbf{m}|\sigma_j|\mathbf{r}\rangle}\,. \tag{4.6}$$

Again, they observe that,

$$\Psi_{\mathbf{m}}((\sigma_b, \mathbf{n})\mathbf{r}) = \Psi_{\mathbf{m}}(\mathbf{r}) = \Psi_{\sigma_b \cdot \mathbf{m}}(\mathbf{r})\,, \tag{4.7}$$

from which they conclude that with σ_b, a reflection operator of one of the cavity's boundaries, the normal derivative, $(\hat{\mathbf{n}}_\mathbf{b} \cdot \nabla)\Psi_{\mathbf{m}}(\mathbf{r})$ vanishes when $\mathbf{r}$ or $\mathbf{m}$ lies on the

mentioned boundary. This differs from the Dirichlet case, because one does not get a similar explicit null constraint on the mode numbers for $\Psi_{\mathbf{m}}(\mathbf{r})$ itself but rather for its normal derivative. These Neumann modes are unphysical when all mode numbers are simultaneously null, $\mathbf{m} = \mathbf{0}$.

4.2.3 Eigenvalues and Completeness

From Eqs. (4.4) and (4.6), one easily obtains the Laplacian eigenvalues (Eq. (2.13)),

$$\lambda_{\mathbf{m}}^2 = 4\pi^2 \langle \mathbf{m}|\mathbf{m}\rangle \,, \tag{4.8}$$

in terms of the norm of the dual lattice vector. The same eigenvalue form is obtained for both boundary conditions but with different constraints on the mode numbers. How does one demonstrate that the set of eigenfunctions is complete? Terras and Swanson consider Dirichlet modes as an example. Let us assume a function $f(\mathbf{r})$ that vanishes on the boundaries of the domain V. It is well known in lattice Fourier theory, that a function which is invariant under a set of integral spatial translations $\mathbf{n} \in L$,

$$f(\mathbf{r} + \mathbf{n}) = f(\mathbf{r}) \,, \tag{4.9}$$

may be written as a Fourier series of the form,

$$f(\mathbf{r}) = \frac{1}{v(\mathbf{R})} \sum_{\mathbf{m}\in L'} \hat{f}(\mathbf{m})\, e^{-2\pi i \langle \mathbf{m}|\mathbf{r}\rangle} \,, \tag{4.10}$$

where $\mathbf{m}$ belongs to the set of dual vectors, and $v(\mathbf{R})$ denotes the volume of the primitive cell associated with the vectors $\mathbf{n}$ [49, 50]. From simple Fourier analysis, one can determine the coefficient,

$$\hat{f}(\mathbf{m}) = \int_{\mathbf{R}} f(\mathbf{r})\, e^{2\pi i \langle \mathbf{m}|\mathbf{r}\rangle} d\mathbf{r} \,. \tag{4.11}$$

Now, defining an alternating extension of a function g over space such that,

$$g((\sigma, \mathbf{n})\mathbf{r}) = \det(\sigma)\, g(\mathbf{r})\,, \tag{4.12}$$

one notes that if f, of Eq. (4.10), is similarly extended in an alternating fashion, one obtains,

$$f(\mathbf{r}) = \frac{1}{n_S\, v(\mathbf{R})} \sum_{\mathbf{m}\in L'} \hat{f}(\mathbf{m})\, \Phi^*_{\mathbf{m}}(\mathbf{r})\,, \tag{4.13}$$

using Eq. (4.4), and n_S which is the order of the point group S. It follows then that,

$$\hat{f}(\mathbf{m}) = \int_{\mathbf{V}} f(\mathbf{r})\, \Phi^*_{\mathbf{m}}(\mathbf{r}) d\mathbf{r}\,. \tag{4.14}$$

Although this may appear to be sufficient to show the completeness of Dirichlet eigenfunctions, there is still a need to make sure that every dual vector $\mathbf{m}$ maps to a unique eigenfunction $\Phi_{\mathbf{m}}$. It was noted earlier in Eq. (4.5) that $\Phi_{\mathbf{m}}$ and $\Phi_{\sigma_b\cdot\mathbf{m}}$ differ at most by a sign. Hence, if one were to choose $\mathbf{m}$ to be enclosed in a sector formed by the corner boundaries of the cavity, but not on the boundaries, we would then be able to uniquely define $\Phi_{\mathbf{m}}$. The authors point out that the corner in question is, coincidentally, the cavity's most acute corner. Finally, it has been shown that with the right choice of dual vectors $\mathbf{m}$, the Dirichlet eigenfunctions (Eq. (4.4)) do indeed form a complete set, which one observes in the form of Fourier expansions (Eqs. (4.13) and (4.14)). One would proceed in a similar way for Neumann modes, except this time a symmetric extension would be used instead of an alternating extension,

$$g((\sigma, \mathbf{n})\mathbf{r}) = g(\mathbf{r})\,, \tag{4.15}$$

the mode numbers would be allowed to lie on the bounding planes, and the normalizations would be more complicated.

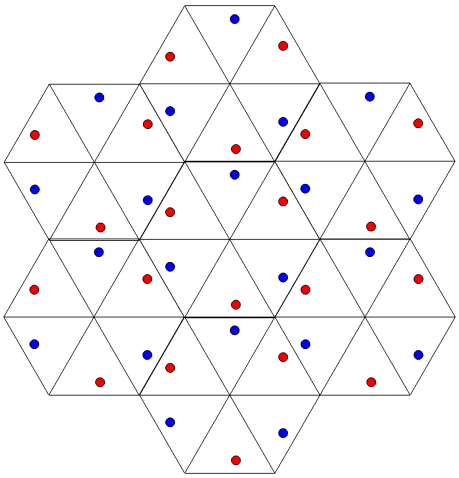

Figure 4.2: Tiling the plane with the hexagonal primitive cells for an equilateral triangle.

4.3 Isoareal and Isoperimetric Quotients

4.3.1 Polygons

The isoperimetric quotient of a closed curve is defined as the ratio of its area A to the area of a circle with the same perimeter P [51],

$$\mathcal{Q} = 4\pi \frac{A}{P^2} \,. \tag{4.16}$$

It has been known for a very long time, since the times of ancient Greece and possibly even earlier, that the circle is a unique curve for which the isoperimetric quotient is maximal, $\mathcal{Q} = 1$. This is commonly known as the *Isoperimetric Inequality* [52], which states that for any closed curve in the plane, $Q \leq 1$. One way to rephrase this is that for a given perimeter the circle encompasses the largest area or conversely, a circle of fixed area has the smallest perimeter of all possible closed curves with the same area. This property of planar curves appears to be of relevance when comparing Casimir energies. Indeed, comparing different shapes, say a square and an ellipse, may not

be unlike comparing an apple to an orange. The best way to do so is to define a dimensionless quantity, which impartially reflects the characteristics of the shapes. The isoperimetic quotient is a very good choice for that purpose.

Another interesting fact about the isoperimetric quotient is that the inequality from which it is derived applies within well-defined geometric classes. For instance the equilateral triangle has the highest $\mathcal{Q}$ amongst all triangles. Likewise, the square has the highest $\mathcal{Q}$ amongst all rectangles. In general, one can show that a regular n-gon has the highest isoperimetric quotient of all n-sided figures [53].

4.3.2 Polyhedrons

Comparing two polyhedrons poses the same problem as polygons. The isoareal quotient $\mathcal{Q}$ of polyhedron is defined as the ratio of its squared volume to that of a sphere with the same surface area S [51]

$$\mathcal{Q} = 36\pi \, \frac{V^2}{S^3} \, . \tag{4.17}$$

This also follows from an equivalent *Isoareal Inequality* which states that of all the closed three-dimensional surfaces, the sphere encloses the largest volume for a given surface area or the converse: $\mathcal{Q} \leq 1$. Again, the isoareal quotient answers the need to objectively compare three-dimensional closed surfaces. It will be of importance when comparing Casimir energies of cavities.

Chapter 5

Casimir Energies of Infinite Prisms and Polygons

There have been many attempts to understand how the vacuum self-energy of a system depends on its geometry or boundaries. After many calculations and results, it appears that the answer may not be intuitive. Nevertheless, one can always formulate interesting hypotheses. If the self-energy of a system does, indeed, depend on its geometry, then suppose we focus on just one aspect. For instance, if one were to consider a set of infinite regular polygonal prisms, how would the vacuum energies evolve as the number of sides increases (Fig.5.1)? Would the result eventually converge to that of a cylinder (circular cross section)? Would results for cylinders of arbitrary cross sections also follow the same behavior? The answers to such questions would very likely advance our search.

The energy of an infinite cylinder of arbitrary cross section will certainly not depend on its length but rather on its cross section or possibly a relation of its cross-sectional attributes. Hence, working with a set of regular polygonal cross sections which displays an interesting transition would be a perfect way to observe this behavior. Such work is feasible, granted that the spectra for these geometries are known or derivable in some way. Naturally, we turn to the integrable triangles and rectangles, whose spectra are known exactly. Of course, one could also expect a similarly interesting behavior for finite prisms or even polygons. We will, in fact, consider those cases. Although, for the moment only for Dirichlet and Neumann boundaries. Cylinders of infinite length with perfectly conducting boundary conditions or waveguides, on the other

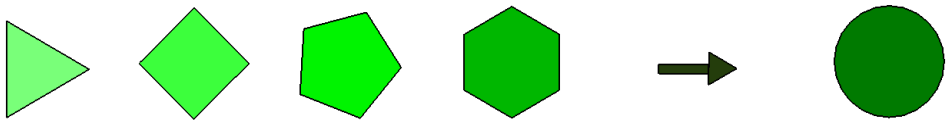

Figure 5.1: Regular polygons. How would the Casimir energies of these regular polygonal prisms evolve?

hand, have long been a subject of interest to engineers and scientists. The solutions for their electromagnetic modes have been shown repeatedly to reduce to two simpler problems: Helmholtz equations for scalar fields satisfying Dirichlet and Neumann boundary conditions [30].

The results we will obtain in the forthcoming sections will be exclusively for the interior of the prisms [21, 23]. This is a shortcoming due to the method of images. Nonetheless, this creates further opportunities to ponder the ramifications.

5.1 Equilateral Triangular Prism

A figure almost obscured by time, Lamé is known for many accomplishments, one being the first to find the Laplacian eigenspectrum for an equilateral triangle [54]. This result has been re-examined or extended in many works [30, 43, 55–58]. The Laplacian eigenvalues for an equilateral triangle bounded by the lines $y = 0$, $y = \sqrt{3}\,x$, and $y = \sqrt{3}\,(a - x)$ are of the form [48]

$$\lambda^2_{\mathbf{m}} = \frac{16\pi^2}{9a^2}(m^2 - m\,n + n^2)\,, \tag{5.1}$$

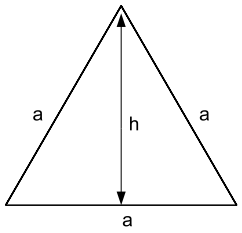

Figure 5.2: Equilateral triangle of side a and height $h = \sqrt{3}a/2$.

where we have chosen a different but equivalent parametrization of Lamé's result. We will also choose to express our results in terms of the height, $h = \sqrt{3}\,a/2$. The integers m and n are positive or negative and satisfy completeness constraints that depend on the boundary conditions.

5.1.1 Dirichlet BC

Following the procedure outlined in Chapter 4, the Dirichlet eigenfunctions fall into two types. The unnormalized eigenfunction (4.4) is reduced into real and imaginary parts [48]

$$\Phi_{\mathbf{m}}(\mathbf{r}) = \alpha_{\mathbf{m}}(\mathbf{r}) + i\,\beta_{\mathbf{m}}(\mathbf{r})\,, \tag{5.2}$$

where

$$\begin{aligned}\alpha_{\mathbf{m}}(\mathbf{r}) = &\sin\left[\frac{2\pi}{3a}(m-2n)x\right]\sin\left[\frac{2\pi}{\sqrt{3}a}my\right] \\ &-\sin\left[\frac{2\pi}{3a}(n-2m)x\right]\sin\left[\frac{2\pi}{\sqrt{3}a}ny\right] \\ &-\sin\left[\frac{2\pi}{3a}(m+n)x\right]\sin\left[\frac{2\pi}{\sqrt{3}a}(m-n)y\right]\,,\end{aligned} \tag{5.3}$$

and

$$\begin{aligned}\beta_{\mathbf{m}}(\mathbf{r}) = &- \cos\left[\frac{2\pi}{3a}(m-2n)x\right]\sin\left[\frac{2\pi}{\sqrt{3}a}my\right] \\ &+ \cos\left[\frac{2\pi}{3a}(n-2m)x\right]\sin\left[\frac{2\pi}{\sqrt{3}a}ny\right] \\ &+ \cos\left[\frac{2\pi}{3a}(m+n)x\right]\sin\left[\frac{2\pi}{\sqrt{3}a}(m-n)y\right]\,.\end{aligned} \tag{5.4}$$

The real modes $\alpha_{\mathbf{m}}$ and $\beta_{\mathbf{m}}$ are both needed to form a complete set. One can see this in the construction of Green's function (2.15):

$$\Phi_{\mathbf{m}}(\mathbf{r})\Phi^*_{\mathbf{m}}(\mathbf{r}') = \alpha_{\mathbf{m}}(\mathbf{r})\alpha_{\mathbf{m}}(\mathbf{r}') + \beta_{\mathbf{m}}(\mathbf{r})\beta_{\mathbf{m}}(\mathbf{r}')\,. \tag{5.5}$$

From these explicit constructions, one can also check that the eigenfunctions vanish for the choices of $m = n$, $m = 0$, and $n = 0$, and are invariant (up to a minus sign) under the 6 symmetry transformations:

$$(x,\, y) \to (x,\, y) \tag{5.6a}$$

$$\to (x,\, -y) \tag{5.6b}$$

$$\to 1/2\,(-x - \sqrt{3}\,y,\, -\sqrt{3}\,x + y) \tag{5.6c}$$

$$\to 1/2\,(-x - \sqrt{3}\,y,\, \sqrt{3}\,x - y) \tag{5.6d}$$

$$\to 1/2\,(-x + \sqrt{3}\,y,\, -\sqrt{3}\,x - y) \tag{5.6e}$$

$$\to 1/2\,(-x + \sqrt{3}\,y,\, \sqrt{3}\,x + y) \tag{5.6f}$$

Without further formalities, we proceed directly with the dimensionally regularized expression (3.18) to give the Casimir energy for Dirichlet boundary conditions,

$$\mathcal{E}_{\rm Eq}^{(D)} = -\frac{\Gamma(-(1+d)/2)}{2^{d+2}\pi^{(d+1)/2}}\left[\frac{4}{3}\left(\frac{\pi}{h}\right)^2\right]^{(d+1)/2} \times \frac{1}{6}\Bigg(\sum_{m,n=-\infty}^{\infty}{}' (m^2 - mn + n^2)^{(1+d)/2} - 6\zeta(-1-d)\Bigg). \tag{5.7}$$

The mode numbers form a complete set when $0 < m < n$. The sum over this set is given in an equivalent form by extending the ranges for m and n over all possible values, subtracting the unphysical cases, and accounting for the 6 degeneracies. The double sum on m and n is exactly of the type examined by Chowla and Selberg [32]. We, therefore, use the Chowla-Selberg formula to obtain a rapidly converging numerical result (see Appendix B). After a few manipulations such as the use of the reflection property (3.19), d is then analytically continued to 1:

$$\mathcal{E}_{\rm Eq}^{(D)} = \frac{1}{144\pi^2 h^2}\Bigg(8\pi\zeta(3) - 3^{3/2}\zeta(4) - 4\pi^2(12)^{3/4}\sum_{n=1}^{\infty} n^{-3/2}(-1)^n \sigma_3(n) K_{3/2}(n\pi\sqrt{3}\,)\Bigg). \tag{5.8}$$

The above expression converges rapidly, reaching an accuracy of twenty decimal places by summing just the first eight terms,

$$\mathcal{E}_{\rm Eq}^{(D)} = \frac{0.017789138469130117062}{h^2}. \tag{5.9}$$

5.1.2 Neumann BC

The Neumann eigenfunctions (4.6) are slightly similar to the Dirichlet eigenfunctions. Again, excecuting the method given in Chapter 4, we obtain a similar breakup into

real and imaginary parts (5.2)

$$\Psi_{\mathbf{m}}(\mathbf{r}) = \gamma_{\mathbf{m}}(\mathbf{r}) + i\,\delta_{\mathbf{m}}(\mathbf{r})\,, \tag{5.10}$$

where,

$$\begin{aligned}\gamma_{\mathbf{m}}(\mathbf{r}) = &\cos\left[\frac{2\pi}{3a}(m-2n)x\right]\cos\left[\frac{2\pi}{\sqrt{3}a}my\right] \\ &+\cos\left[\frac{2\pi}{3a}(n-2m)x\right]\cos\left[\frac{2\pi}{\sqrt{3}a}ny\right] \\ &+\cos\left[\frac{2\pi}{3a}(m+n)x\right]\cos\left[\frac{2\pi}{\sqrt{3}a}(m-n)y\right]\,,\end{aligned} \tag{5.11}$$

and

$$\begin{aligned}\delta_{\mathbf{m}}(\mathbf{r}) = &\sin\left[\frac{2\pi}{3a}(m-2n)x\right]\cos\left[\frac{2\pi}{\sqrt{3}a}my\right] \\ &+\sin\left[\frac{2\pi}{3a}(n-2m)x\right]\cos\left[\frac{2\pi}{\sqrt{3}a}ny\right] \\ &+\sin\left[\frac{2\pi}{3a}(m+n)x\right]\cos\left[\frac{2\pi}{\sqrt{3}a}(m-n)y\right]\,.\end{aligned} \tag{5.12}$$

These real modes, together, also form a complete set. A glance at the previous two equations reveals that they only yield unphysical information when $m = 0 = n$. The completeness constraint is similar to the Dirichlet case: the mode numbers must satisfy $0 \leq m \leq n$, obviously excluding $m = 0 = n$. Summing over these ranges by *symmetrical extension*, which we explained earlier for the Dirichlet calculation, we obtain

$$\mathcal{E}^{(N)}_{\mathrm{Eq}} = \mathcal{E}^{(D)}_{\mathrm{Eq}} - \frac{\zeta(3)}{6\pi h^2} \tag{5.13a}$$

$$= -\frac{0.045982}{h^2}\,. \tag{5.13b}$$

5.1.3 Electromagnetic BC

The Casimir energy per lenth for an electromagnetic field inside an infinitely long equilateral triangular waveguide with perfectly conducting sides is simply the sum of the previous two results:

$$\mathcal{E}_{\text{Eq}}^{(\text{EM})} = \mathcal{E}_{\text{Eq}}^{(D)} + \mathcal{E}_{\text{Eq}}^{(N)} \tag{5.14a}$$

$$= -\frac{0.028193}{h^2}. \tag{5.14b}$$

Note that while the Dirichlet energy is positive, the electromagnetic energy is negative, because the H (TE) mode contribution overwhelms that of the E (TM) mode [30]. Transverse electric TE or H modes are electromagnetic modes where the electric field has no component in the longitudinal direction of the waveguide. The term H mode is equivalent because the corresponding magnetic field has a component in the longitudinal direction. One can extend the same definitions to transverse magnetic (TM) modes, also known as E modes.

5.1.4 Point-splitting Regularization

We have shown how to calculate Casimir energies for an infinite equilateral triangular cylinder using dimensional regularization. Equivalently, one can also use a point-splitting regularization to obtain the same results in addition to explicitly isolating the divergences. First let us apply a transformation on the mode numbers

$$m = r + s \tag{5.15a}$$

$$n = r - s \tag{5.15b}$$

As a result,

$$\lambda_{\mathbf{m}}^2 \to \lambda_{\mathbf{m}}^2 = \frac{16\pi^2}{9a^2}(3\,r^2 + s^2)\,. \tag{5.16}$$

The eigenvalues now appear in a diagonalized form with r and s taking integer as well as half-integer values. Let

$$g(r,s) = e^{-\tau\sqrt{k^2+\lambda_{\mathbf{m}}^2}}\,, \tag{5.17}$$

defined in terms of $\lambda_{\mathbf{m}}^2$ (5.16) and the continuous mode number k. As a function of g, the Dirichlet zero-point energy is of the form:

$$\mathcal{E}_{Eq}^{(D)} = \frac{1}{12}\lim_{\tau\to 0}\left(-\frac{d}{d\tau}\right)\int_{-\infty}^{\infty} dk \sum_{r,s=-\infty}^{\infty}\Big[g(r,s) + g(r+1/2, s+1/2) \\ - 3\,g(0,s) + 2\,g(0,0)\Big]\,. \tag{5.18}$$

By definition, if one or more of the arguments of g are null then the sums are only over the other arguments. For example, the sum over $g(0,s)$ would only be over s, and $g(0,0)$ would not be summed over. We can now freely use the regularization formulas derived earlier in Chapter 3. Using Eqs. (3.8), (3.9), and (3.10), we quickly isolate the divergent parts:

$$\frac{\sqrt{3}\,h^2}{\pi^2\tau^4} - \frac{\sqrt{3}\,h}{2\pi\tau^3} + \frac{1}{3\pi\tau^2} = 2\left(\frac{3A}{2\pi^2\tau^4} - \frac{P}{8\pi\tau^3} + \frac{C}{48\pi\tau^2}\right)\,. \tag{5.19}$$

We note that the volume and surface divergent terms, which are respectively proportional to the area of the triangle $A = h^2/\sqrt{3}$ and the perimeter $P = 2\sqrt{3}\,h$, are as expected, and are presumably not of physical relevance. The last term, a constant in h, certainly does not contribute to the self-stress on the cylinder. Only this term reflects the corner divergences, and for the equilateral triangle we have $C = 8$ (3.14).

The finite part is also easily extracted and simplified:

$$\mathcal{E}_{\rm Eq}^{(D)} = \frac{1}{144\pi^2 h^2}\left(12\pi\zeta(3) - \frac{10\sqrt{3}}{3}\zeta(4) - \frac{16\sqrt{3}}{3}\sum_{p,q=1}^{\infty}\frac{1+(-1)^{p+q}}{(p^2+q^2/3)^2}\right). \tag{5.20}$$

The double sum in the above expression converges slowly. Directly summing the first 500 terms for m and n, we only reach a seven-decimal accuracy,

$$\mathcal{E}_{\rm Eq}^{(D)} = \frac{0.0177891}{h^2}, \tag{5.21}$$

which, regardless, agrees with Eq. (5.9). Because of the numerical agreement, one is convinced that both regularization methods yield exactly the same answer and we have thus shown that our calculations are correct and consistent.

A virtue of the alternative form (5.20) is that it is now evident from Eq. (5.13a) that in the electromagnetic energy (5.14a) the $\zeta(3)$ term completely cancels. As a result, the electromagnetic energy is manifestly negative. This is a feature that will persist in all the calculations for infinite prisms.

5.1.5 Closed-form Result

Although the consistency of two regularization methods is already sufficient, there is yet a third and more impressive approach which gives closed-form results. Following Refs. [35–39], we write for the equilateral triangular cross section, from Eq. (3.18),

$$\mathcal{E}_{\rm Eq}^{(D)} = -\lim_{s\to -1}\frac{1}{2}(4\pi)^s\,\Gamma(s)\left(\frac{4\pi^2}{3h^2}\right)^{-s}\left[\zeta(s)L_{-3}(s) - \zeta(2s)\right], \tag{5.22}$$

in terms of the single series

$$L_{-3}(s) = \sum_{n=0}^{\infty}\left[\frac{1}{(3n+1)^s} - \frac{1}{(3n+2)^s}\right]. \tag{5.23}$$

Now, this function satisfies the reflection property

$$L_{-3}(s)\Gamma(s) = \frac{\sqrt{3}\,(2\pi/3)^s}{2\cos(s\pi/2)} L_{-3}(1-s). \tag{5.24}$$

Then, using Eq. (3.19), we can take the limit $s \to -1$:

$$\mathcal{E}_{\rm Eq}^{(D)} = -\frac{1}{96h^2}\left[\sqrt{3}\,L_{-3}(2) - \frac{8}{\pi}\zeta(3)\right]. \tag{5.25}$$

In fact, the remaining sum has a closed form:

$$L_{-3}(2) = \frac{1}{9}\left[\psi'(1/3) - \psi'(2/3)\right], \tag{5.26}$$

in terms of the polygamma function. Thus

$$\mathcal{E}_{\rm Eq}^{(D)} = -\frac{1}{96h^2}\left[\frac{\sqrt{3}}{9}\left[\psi'(1/3) - \psi'(2/3)\right] - \frac{8}{\pi}\,\zeta(3)\right] = \frac{0.0177891}{h^2}. \tag{5.27}$$

It is *a priori* remarkable that such an explicit form can be achieved for a strong-coupling problem.

In particular, from Eqs. (5.13a) and (5.14a), we see that the interior Casimir energy for a perfectly conducting cylinder with equilateral triangular cross section has the simple form

$$\mathcal{E}_{\rm Eq}^{(\rm EM)} = -\frac{\sqrt{3}}{432\,h^2}[\psi'(1/3) - \psi'(2/3)], \tag{5.28}$$

that is, as we noted above, the $\zeta(3)$ cancels.

5.2 Hemiequilateral Triangular Prism

The hemiequilateral triangle or 30°-60°-90° triangle (Fig. 5.3) has an interesting relation to the equilateral triangle as its name suggests. Let us, then, consider a hemiequilateral

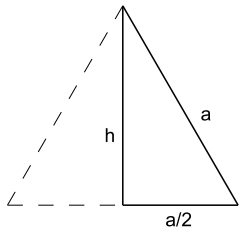

Figure 5.3: Hemiequilateral triangle obtained by bisecting an equilateral triangle.

domain defined by the boundaries: $y = 0$, $y = x/\sqrt{3}$, and $y = \sqrt{3}\,(a - x)$. It is obtained by halving the equilateral triangle of the previous section along one of its three symmetry lines, $y = x/\sqrt{3}$. This relation between the two triangular figures, however, extends further than their geometrical constructions into the realm of zero-point energies. In fact, to start with, they share the same eigenvalue form:

$$\lambda^2_{\mathbf{m}} = \frac{16\pi^2}{9a^2}(m^2 - m\,n + n^2)\,, \tag{5.29}$$

albeit, with different constraints. The energies are also related, which means that the hemiequilateral Casimir energies can also be given in closed-form. In our calculations, we will often replace a with the height $h = \sqrt{3}\,a/2$ as the scale parameter.

5.2.1 Dirichlet BC

By simple observation, one can postulate that the Dirichlet eigenfunctions for the hemiequilateral triangle could be a subset of the equilateral triangle's. This subset would be chosen such that the modes would vanish on the height common to both

triangles. An explicit construction of the modes quickly confirms this postulate:

$$\begin{aligned}\Phi_{\mathbf{m}}(\mathbf{r}) = &\sin\left[\frac{2\pi}{3a}(m-2n)x\right]\sin\left[\frac{2\pi}{\sqrt{3}a}my\right] \\ &-\sin\left[\frac{2\pi}{3a}(n-2m)x\right]\sin\left[\frac{2\pi}{\sqrt{3}a}ny\right] \\ &-\sin\left[\frac{2\pi}{3a}(m+n)x\right]\sin\left[\frac{2\pi}{\sqrt{3}a}(m-n)y\right]\,.\end{aligned} \tag{5.30}$$

This is one of the modes for the Dirichlet equilateral (5.4), and it is the type that vanishes on the chosen perpendicular bisector. The mode numbers form a complete set when $n < m < 2n$. Accounting for the 12 symmetries and 6 unphysical modes $\{m = \pm n, m = 0, n = 0, m = 2n, n = 2m\}$, the Casimir energy is obtained and simplified in terms of the Dirichlet equilateral result:

$$\mathcal{E}^{(D)}_{369} = \frac{\mathcal{E}^{(D)}_{\text{Eq}}}{2} + \frac{\zeta(3)}{8\pi h^2} = \frac{0.0567229}{h^2}\,, \tag{5.31}$$

again, a positive energy.

5.2.2 Neumann BC

The Neumann modes also follow suit:

$$\begin{aligned}\Psi_{\mathbf{m}}(\mathbf{r}) = &\cos\left[\frac{2\pi}{3a}(m-2n)x\right]\cos\left[\frac{2\pi}{\sqrt{3}a}my\right] \\ &+\cos\left[\frac{2\pi}{3a}(n-2m)x\right]\cos\left[\frac{2\pi}{\sqrt{3}a}ny\right] \\ &+\cos\left[\frac{2\pi}{3a}(m+n)x\right]\cos\left[\frac{2\pi}{\sqrt{3}a}(m-n)y\right]\,.\end{aligned} \tag{5.32}$$

They are a subset of the equilateral Neumann modes (5.12), whose normal derivatives vanish on the common height. The completeness properties are also similar to the

corresponding Dirichlet's: $n \leq m \leq 2n$ excluding the possibility of $m = 0 = n$. By symmetrical extension, we promptly write the zero-point energy, which we simplify in terms of Eq. (5.13a):

$$\mathcal{E}_{369}^{(N)} = \frac{\mathcal{E}_{\text{Eq}}^{(N)}}{2} - \frac{\zeta(3)}{8\pi h^2} = -\frac{0.0708193}{h^2}, \tag{5.33}$$

which is again negative.

5.2.3 Electromagnetic BC

The electromagnetic Casimir energy in the interior of an infinitely long cylinder of hemiequilateral triangular cross section follows directly by adding the E and H mode contributions,

$$\mathcal{E}_{369}^{(\text{EM})} = \mathcal{E}_{369}^{(D)} + \mathcal{E}_{369}^{(N)} = \frac{1}{2}\mathcal{E}_{\text{Eq}}^{(\text{EM})} = -\frac{0.0140964}{h^2}, \tag{5.34}$$

which is, remarkably, exactly one-half that of the energy of equilateral triangle, as might have been anticipated naively.

5.3 Square Prism

Infinite prisms with square cross sections have long been considered for self-energy calculations. The results we present here mirror a few previous works [16,19]. However, it appears it has never been really appreciated that the self-energies for these infinite square cylinders can be given in closed-form (Lukosz actually gives a closed-form electromagnetic result as a limit from a finite prism [16]). We consider a square of side length a formed by the lines $x = 0$, $x = a$, $y = 0$, and $y = a$. The eigenvalues for

this geometry are of the simplest quadratic form,

$$\lambda_{\mathbf{m}}^2 = \frac{\pi^2}{a^2}\left(m^2+n^2\right)\,. \tag{5.35}$$

This is a well-known result, as it appears in nearly every textbook on electromagnetism.

5.3.1 Dirichlet BC

The Dirichlet eigenfunctions for a square boundary are just as predictable:

$$\Phi_{\mathbf{m}}(\mathbf{r}) = \sin\left(\frac{2\pi}{a}mx\right)\sin\left(\frac{2\pi}{a}ny\right)\,. \tag{5.36}$$

For completeness, the mode numbers must be positive $m>0$ and $n>0$. With two unphysical modes $\{m=0,n=0\}$, and a degeneracy of 4, we proceed just as in the previous cases

$$\begin{aligned}
\mathcal{E}_{\mathrm{Sq}}^{(D)} &= -\frac{1}{32\pi^2a^2}\left[2\zeta(4)-\pi\zeta(3)+8\pi^2\sum_{l=1}^{\infty}l^{-3/2}\sigma_3(l)K_{3/2}(\pi l)\right] && \text{(5.37a)}\\
&= -\frac{1}{32\pi^2a^2}\left[4\zeta(4)-2\pi\zeta(3)+4\sum_{k,l=1}^{\infty}\frac{1}{(k^2+l^2)^2}\right] && \text{(5.37b)}\\
&= 0.00483155/a^2\,, && \text{(5.37c)}
\end{aligned}$$

whereby we obtain a result consistent with Refs. [16, 19]. The closed-form result may be obtained directly from the double sum [33, 34, 36],

$$\sum_{k,l=1}^{\infty}\frac{1}{(k^2+l^2)^2} = \zeta(2)L_{-4}(2)-\zeta(4), \tag{5.38}$$

where

$$L_{-4}(2) = \sum_{m=0}^{\infty}\frac{(-1)^m}{(2m+1)^2} = G. \tag{5.39}$$

The constant $G = 0.915966\ldots$ is the well-known Catalan's constant. Then

$$\mathcal{E}_{\text{Sq}}^{(D)} = \frac{1}{16\pi a^2}\left[\zeta(3) - \frac{\pi}{3}G\right] = \frac{0.00483155}{a^2}. \tag{5.40}$$

5.3.2 Neumann BC

The Neumann modes are also simple:

$$\Psi_{\mathbf{m}}(\mathbf{r}) = \cos\left(\frac{2\pi}{a}mx\right)\cos\left(\frac{2\pi}{a}ny\right). \tag{5.41}$$

Instead of sines (5.36) we now have cosines. The completeness constraints allow the mode numbers to be null $m \geq 0$ and $n \geq 0$ but not simultaneously. The Neumann energy in relation to the Dirichlet energy is

$$\mathcal{E}_{\text{Sq}}^{(N)} = \mathcal{E}_{\text{Sq}}^{(D)} - \frac{\zeta(3)}{8\pi a^2} = -\frac{0.0429968}{a^2}, \tag{5.42}$$

which again reproduces the known result.

5.3.3 Electromagnetic BC

Summing Dirichlet and Neumann energies, we obtain the following electromagnetic Casimir energy for the interior of a perfectly conducting square waveguide, expressed only in terms of one transcendental number G:

$$\mathcal{E}_{\text{Sq}}^{(\text{EM})} = \mathcal{E}_{\text{Sq}}^{(D)} + \mathcal{E}_{\text{Sq}}^{(N)} = -\frac{G}{24a^2} = -\frac{0.0381653}{a^2}. \tag{5.43}$$

5.4 Right Isosceles Triangular Prism

The geometric relation of the isosceles right triangle to the square is analogous to that of the hemiequilateral triangle to the equilateral triangle. Cutting along a square

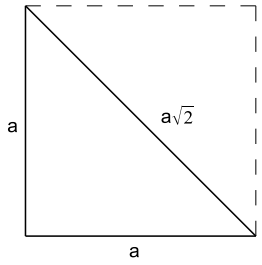

Figure 5.4: Isosceles right triangular waveguide, of side a.

diagonal produces an isosceles triangle (Fig. 5.4). Our triangle in question has for boundaries $y = 0$, $x = a$, and $y = x$. It has the same eigenvalue form as its matching square,

$$\lambda_{\mathbf{m}}^2 = \frac{\pi^2}{a^2}\left(m^2 + n^2\right) , \tag{5.44}$$

although, the right isosceles triangle modes are not exactly a subset of the square's. Rather, they are a linear combination of the latter [30, 43, 48].

5.4.1 Dirichlet BC

The Dirichlet characteristic modes are of the form:

$$\Phi_{\mathbf{m}}(\mathbf{r}) = \sin\left(\frac{2\pi}{a}mx\right)\sin\left(\frac{2\pi}{a}ny\right) - \sin\left(\frac{2\pi}{a}my\right)\sin\left(\frac{2\pi}{a}nx\right) . \tag{5.45}$$

This particular combination of the square modes (5.36) is made so that Φ vanishes when $x = y$. For completeness, m and n must satisfy $m > n > 0$. Just as in the previous cases, the self-energy follows seamlessly. The sums over these ranges are symmetrically extended over all values while the unphysical modes $\{m = 0, n = 0, m = \pm n\}$ are removed and the 8 degeneracies are taken into account. The Casimir energy can be

related to that of the Dirichlet square,

$$\mathcal{E}_{\rm Iso}^{(D)} = \frac{\mathcal{E}_{\rm Sq}^{(D)}}{2} + \frac{\zeta(3)}{16\pi a^2} = \frac{0.0263299}{a^2}\,, \tag{5.46}$$

a positive number again.

5.4.2 Neumann BC

The Neumann modes are symmetric under the exchange $x \leftrightarrow y$,

$$\Psi_{\mathbf{m}}(\mathbf{r}) = \cos\left(\frac{2\pi}{a}mx\right)\cos\left(\frac{2\pi}{a}ny\right) + \cos\left(\frac{2\pi}{a}my\right)\cos\left(\frac{2\pi}{a}nx\right)\,, \tag{5.47}$$

and are unphysical only when $m = 0 = n$. The modes form a complete set for $m \geq n \geq 0$ without $m = 0 = n$. The relation of the Neumann self-energy to the square's is then,

$$\mathcal{E}_{\rm Iso}^{(N)} = \frac{\mathcal{E}_{\rm Sq}^{(N)}}{2} - \frac{\zeta(3)}{16\pi a^2} = -\frac{0.0454125}{a^2}, \tag{5.48}$$

again a negative number.

5.4.3 Electromagnetic BC

We combine both results to obtain the electromagnetic Casimir energy for a perfectly conducting waveguide of right isosceles triangular cross section,

$$\mathcal{E}_{\rm Iso}^{\rm (EM)} = \mathcal{E}_{\rm Iso}^{(D)} + \mathcal{E}_{\rm Iso}^{(N)} = \frac{1}{2}\mathcal{E}_{\rm Sq}^{\rm (EM)} = -\frac{G}{48a^2} = -\frac{0.0190826}{a^2}, \tag{5.49}$$

again a remarkably simple and unexpected result.

Cross section	$\mathcal{E}^{(\mathrm{D,N})}$	$\mathcal{E}^{(\mathrm{EM})}$
Hemiequilateral Tr.	$\left[\pm 32\zeta(3) - \pi\sqrt{3}L_{-3}(2)\right]/192\pi h^2$	$-\sqrt{3}L_{-3}(2)/96h^2$
Isosceles Right Tr.	$\left[\pm 9\zeta(3) - \pi G\right]/96\pi a^2$	$-G/48a^2$
Equilateral Tr.	$\left[\pm 8\zeta(3) - \pi\sqrt{3}L_{-3}(2)\right]/96\pi h^2$	$-\sqrt{3}L_{-3}(2)/48h^2$
Square	$\left[\pm 3\zeta(3) - \pi G\right]/48\pi a^2$	$-G/24a^2$

Table 5.1: Casimir energies per unit length (in closed-form) for cylinders of integrable polygonal cross sections. The second and third columns give the Dirichlet, Neumann, and EM (perfectly conducting) energies per length. The $+/-$ signs match with $\mathcal{E}^{(\mathrm{D})}/\mathcal{E}^{(\mathrm{N})}$.

5.5 Rectangular Prisms

The square prism is just a particular element of the class of rectangular prisms, where the side lengths are not necessarily equal. We take the liberty to explore this more general geometry for a better understanding. For that matter, we consider an arbitrary rectangle of side lengths a and b bounded by the lines $x = 0$, $x = a$, $y = 0$, and $y = b$. The characteristic values of the Laplacian are then

$$\lambda_{\mathbf{m}}^2 = \pi^2 \left(\frac{m^2}{a^2} + \frac{n^2}{b^2} \right) , \tag{5.50}$$

an obvious generalization of the square's eigenvalues.

5.5.1 Dirichlet BC

The Dirichlet eigenfunctions are also more general:

$$\Phi_{\mathbf{m}}(\mathbf{r}) = \sin\left(\frac{2\pi}{a}mx\right)\sin\left(\frac{2\pi}{b}ny\right) . \tag{5.51}$$

An arbitrary rectangle has the same modal constraints and degeneracies as a square, which allows us to evaluate the self-energy:

$$\mathcal{E}^{(D)}_{\text{Rect}} = -\frac{1}{32\pi^2 ab}\left[-\pi\frac{b}{a}\zeta(3) + 2\zeta(4) + 8\pi^2\left(\frac{b}{a}\right)^{1/2}\sum_{l=1}^{\infty} l^{-3/2}\sigma_3(l)K_{3/2}(2\pi lb/a)\right] \tag{5.52a}$$

$$\begin{aligned}=&\frac{1}{32\pi^2 a^2}\left[\left(1+\left(\frac{a}{b}\right)^2\right)\pi\zeta(3) - 2\left(\left(\frac{a}{b}\right)^3 + \frac{b}{a}\right)\zeta(4)\right.\\ &\left. - 4\left(\frac{a}{b}\right)^3\sum_{m,n=1}^{\infty}\left(m^2 + \left(n\frac{a}{b}\right)^2\right)^{-2}\right] .\end{aligned} \tag{5.52b}$$

For $a = b$, a square, the Dirichlet energy is positive, but when one side is much larger than the other, the sign of the energy must change, for that situation corresponds to the classic case of Casimir attraction. The Dirichlet Casimir energy vanishes for $b/a = 1.74437$, and is negative for larger values of b/a. See Fig. 5.8a below. Note that for a general rectangle, $a \neq b$, a closed-form expression for the energy is apparently not achievable [37].

5.5.2 Neumann BC

The Neumann characteristic functions are

$$\Psi_{\mathbf{m}}(\mathbf{r}) = \cos\left(\frac{2\pi}{a}mx\right)\cos\left(\frac{2\pi}{b}ny\right) . \tag{5.53}$$

They also, obviously, share the same modal constraints as the square. So, as always, we expres the Neumann energy in terms of the Dirichlet result

$$\mathcal{E}^{(N)}_{\text{Rect}} \;=\; \mathcal{E}^{(D)}_{\text{Rect}} - \left(1+\left(\frac{a}{b}\right)^2\right)\frac{\zeta(3)}{16\pi a^2}\,. \tag{5.54}$$

5.5.3 Electromagnetic BC

Although, we cannot give a closed-form expression for the electromagnetic energy of an arbitrary rectangular cavity, we can nonetheless say that it is always negative. From (5.54) and (5.52b), it is clear that the $\zeta(3)$ terms are cancelled in the sum and the overall result is negative,

$$\mathcal{E}^{(EM)}_{\text{Rect}} = -\frac{1}{8\pi^2 a^2}\left[\left(\left(\frac{a}{b}\right)^3+\frac{b}{a}\right)\zeta(4)+2\left(\frac{a}{b}\right)^3\sum_{m,n=1}^{\infty}\left(m^2+\left(n\frac{a}{b}\right)^2\right)^{-2}\right]. \tag{5.55}$$

One can also note that the results (all three boundary conditions) for the square are recovered when $a=b$.

5.5.4 Closed-form Results

For select values of the ratio a/b, we can give the zero-point energies for rectangles in closed-form. By closed-form, we mean that the expression for the energy may be simplified into a product of known and simpler transcendental functions. Based largely on the extensive work of Glasser and Zucker [37], it has been shown that certain Epstein zeta functions of quadratic forms can be written as products of Dirichlet L-series, some of which can be further simplified for certain arguments. For example, the values of $(a/b)^2 = \{1,2,3,4,5,6,7,8,9,10,12,13,15,16,18,\ldots\}$ all admit simplified forms. Note that the sequence of these numbers is not particularly enlightening; the

reason why one can perform reductions for these particular numbers has to do with number theory and it is almost a felicitous coincidence that we have a contiguous sequence from 1 to 10. So far, the largest known number for $(a/b)^2$ is 1848 with sporadic stretches of contiguous numbers in between.

5.6 Circular Cylinder

The overall goal of these calculations is to detect a correlation between zero-point energies and the varying cross sections of cylinders. It almost goes without saying that the most symmetrical of all cross sections, the circle, must also be included. This configuration was one of the earliest to be considered after Boyer's work on the spherical shell [20, 59–61]. We will not delve into the details of calculations, but point out the crucial fact that just like the spherical shell, the zero-point energies for the circular cylinder include both interior and exterior contributions. A more accurate description would actually be *circular cylindrical shell*.

Interior and exterior contributions are needed because otherwise a finite energy cannot be calculated. Due to the non-zero curvature, one encounters a logarithmic term which adds to the interior energy. Therefore, it is difficult to unambiguously find the energy because of this arbitrary scale. Furthermore, this logarithmic term only vanishes when both interior and exterior energies are added. In essence, the opposite signs for the curvatures on the interior and exterior cancel. The Dirichlet and Neumann self-energies for a circular cylindrical shell of radius a are [15, 59]:

$$\mathcal{E}^{(\mathrm{D})}_{\mathrm{Circ}} = \frac{0.000606}{a^2}\,, \tag{5.56a}$$

$(a/b)^2$	$\mathcal{E}^{(D,N)}_{\text{Rect}} \times (32\pi^2 a^2)$	$\mathcal{E}^{(EM)}_{\text{Rect}} \times (32\pi^2 a^2)$
1	$\pm 2\zeta(3) - 4\zeta(2)L_{-4}(2)$	$-8\zeta(2)L_{-4}(2)$
2	$\pm 3\zeta(3) - 2\zeta(2)L_{-8}(2)$	$-4\zeta(2)L_{-8}(2)$
3	$\pm 4\zeta(3) - \frac{9}{4}\zeta(2)L_{-3}(2)$	$-\frac{9}{2}\zeta(2)L_{-3}(2)$
4	$\pm 5\zeta(3) - \frac{7}{4}\zeta(2)L_{-4}(2)$	$-\frac{7}{2}\zeta(2)L_{-4}(2)$
5	$\pm 6\zeta(3) - \zeta(2)L_{-20}(2) - L_{-4}(2)L_5(2)$	$-2\zeta(2)L_{-20}(2) - 2L_{-4}(2)L_5(2)$
6	$\pm 7\zeta(3) - \zeta(2)L_{-24}(2) - L_{-3}(2)L_8(2)$	$-2\zeta(2)L_{-24}(2) - 2L_{-3}(2)L_8(2)$
7	$\pm 8\zeta(3) - \frac{5}{4}\zeta(2)L_{-7}(2)$	$-\frac{5}{2}\zeta(2)L_{-7}(2)$
8	$\pm 9\zeta(3) - \zeta(2)L_{-24}(2) - L_{-3}(2)L_8(2)$	$-2\zeta(2)L_{-24}(2) - 2L_{-3}(2)L_8(2)$
9	$\pm 10\zeta(3) - \frac{10}{9}\zeta(2)L_{-4}(2) - L_{-3}(2)L_{12}(2)$	$-\frac{20}{9}\zeta(2)L_{-4}(2) - 2L_{-3}(2)L_{12}(2)$
10	$\pm 11\zeta(3) - \zeta(2)L_{-40}(2) - L_5(2)L_{-8}(2)$	$-2\zeta(2)L_{-40}(2) - 2L_5(2)L_{-8}(2)$

Table 5.2: Table of closed-form energies for infinite rectangular prisms. The results for Dirichlet, Neumann, and electromagnetic boundary conditions, scaled by $32\pi^2 a^2$, are given for values of $(a/b)^2$ ranging from 1 to 10. The first row, $(a/b) = 1$, corresponds to the infinite square prism. The $+/-$ signs match respectively to *Dirichlet/Neumann* results.

$$\mathcal{E}_{\text{Circ}}^{(\text{N})} = -\frac{0.01416}{a^2}\,, \tag{5.56b}$$

which together give the electromagnetic result [20]:

$$\mathcal{E}_{\text{Circ}}^{(\text{EM})} = -\frac{0.01356}{a^2}\,. \tag{5.57}$$

5.7 Casimir Energies of Polygons

The Casimir energies for integrable polygons may be readily obtained from the previous results. In fact, the dimensionally regularized expressions, for example Eq. (5.22), allow us simply to take the limit $s \to -1/2$ (for a prism of null length $d \to 0$). The results could then be expressed in terms of Dirichlet L-series. Alternatively, the sums

$$E = \frac{1}{2}\sum_{\mathbf{m}} \sqrt{\lambda_{\mathbf{m}}^2}\,, \tag{5.58}$$

may also be performed directly using the Chowla-Selberg formula for numerical results, which we list in Table 5.5. The results for the square (Dirichlet and Neumann) and the equilateral triangle (Dirichlet) agree with previous calculations [19, 44].

5.8 Analysis

Now, that we have obtained all these results for different cylinders and polygons, how does one make sense of them? First, the energies have an explicit dependence on a physical parameter of the concerned geometry. To put these energies on an equal footing we must somehow scale these energies. Second, how should we compare different geometries impartially?

Cross section	$E^{(\mathrm{D,N})}$
Hemiequilateral Tr.	$\left[\pm\left(1+\sqrt{3}\right)+12\zeta(-1/2)L_{-3}(-1/2)\right]\pi/24\sqrt{3}h$
Isosceles Right Tr.	$\left[\pm\left(1+\sqrt{2}\right)+12\zeta(-1/2)L_{-4}(-1/2)\right]\pi/48a$
Equilateral Tr.	$\left[\pm1+12\zeta(-1/2)L_{-3}(-1/2)\right]\pi/12\sqrt{3}h$
Square	$\left[\pm1+12\zeta(-1/2)L_{-4}(-1/2)\right]\pi/24a$

Table 5.3: Casimir energies (in closed-form) for integrable polygons. The second column gives the Dirichlet and Neumann energies. The $+/-$ signs are matched with $\mathcal{E}^{(\mathrm{D})}/\mathcal{E}^{(\mathrm{N})}$. The parameter h denotes the height for the figures derived from the equilateral triangle, and a represents the side length for the figures derived from the square.

Let us consider the cylinders to start with. The energies per length for cylinders are all of the form C/a^2, where a is a length parameter of the system. One way, also the most intuitive, is to rid the energies of this explicit dependence by scaling them with the cross-sectional area A:

$$\mathcal{E}_{sc} = \mathcal{E} \times A\,. \tag{5.59}$$

To compare different cross sections, we employ the well-known isoperimetric quotient Q (4.16). The scaled energies and isoperimetric quotients are given in Table 5.4. They are then plotted in Fig. 5.5. The curve corresponding to the Dirichlet energies displays a strong systematic behavior while the Neumann and electromagnetic curves develop dubious cusps on the square's data point. This may be related to the fact that energies plotted for the circular cylinder result from interior and exterior contributions. The

Cross section	$\mathcal{E}^{(D)} \times A$	$\mathcal{E}^{(N)} \times A$	$\mathcal{E}^{(EM)} \times A$	$4\pi \times A/P^2$
Hemiequilateral Tr.	0.0163745	−0.0204438	−0.00406928	0.4860
Isosceles Right Tr.	0.0131650	−0.0227063	−0.00954135	0.5390
Equilateral Tr.	0.0102705	−0.0265477	−0.0162772	0.6046
Square	0.00483155	−0.0429968	−0.0381653	0.7854
Circle	0.001904	−0.044485	−0.042581	1

Table 5.4: Casimir energies per unit length for cylinders of various cross sections. The second, third, and fourth columns give the Dirichlet, Neumann, and electromagnetic (perfectly conducting) energies/length multiplied by the cross sectional area. The fifth column gives the isoperimetric quotient of the cross section. All results refer to interior contributions only, with the exception of the final row, which gives the energies for a shell of circular cross section including both interior and exterior modes.

question remains as how to obtain an unambiguous finite energy for just interior modes. This will be addressed at a later time. Nevertheless, it is quite amazing that we are able to observe such order in the graphs.

The situation is very similar for integrable polygons. After all, these polygons share the same cross sections with the cylinders. One notable difference, however, is that the zero-point energy for a disk cannot be determined unambiguously even when both interior and exterior modes are taken into account: one encounters an additional logarithmic scale. Therefore, we work only with the integrable triangles

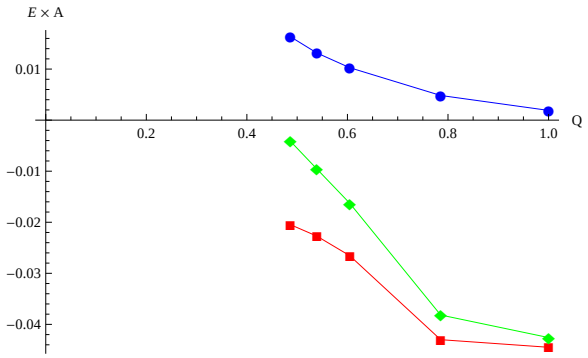

Figure 5.5: Graph of the interior Casimir energy per unit length $\mathcal{E}$ for cylindrical waveguides with various cross sections, multiplied by the cross-sectional area A. These are plotted as a function of the dimensionless isoperimetric quotient $\mathcal{Q} = 4\pi \times A/P^2$. The points shown are for the triangles (hemiequilateral, right isosceles, and equilateral) and the square. The last point is for a circle, including both interior and exterior modes. The upper curve shows the energy for E modes (Dirichlet), the lower curve the energy for H modes (Neumann), and the intermediate curve the energy for the sum of the two modes, that is, for a perfectly conducting cylinder.

Cross section	$E^{(D)}$	$E^{(N)}$	$4\pi \times A/P^2$
Hemiequilateral Tr.	$0.174790/h$	$-0.238159/h$	0.4860
Isosceles Right Tr.	$0.113080/a$	$-0.202939/a$	0.5390
Equilateral Tr.	$0.0877806/h$	$-0.214519/h$	0.6046
Square	$0.0410406/a$	$-0.220759/a$	0.7854

Table 5.5: Casimir energies for plane figures. The second and third columns give the Dirichlet and Neumann energies, expressed in terms of the height h for the figures derived from the equilateral triangle, and the side a for the figures derived from the square. The fourth column gives the isoperimetric quotient of the cross section. All results refer to interior contributions only.

and the square (Table 5.5). The energies are scaled by multiplying them with the square-root of the area:

$$E_{sc} = E \times \sqrt{A}\,. \tag{5.60}$$

We, then, plot these scaled energies against the isoperimetric quotients. The curves in Fig. 5.6 are exemplary in their systematic behavior.

Although it is easy to dismiss rectangles amidst these calculations, they are nonetheless integrable geometries and provide further data. They also differ from the other shapes by the fact that they have two independent lengths: a and b. The other figures only have one. Scaling the energies is rather straightforward, but reducing two parameters to one is trickier. We, first, note that the scaled energies depend on the

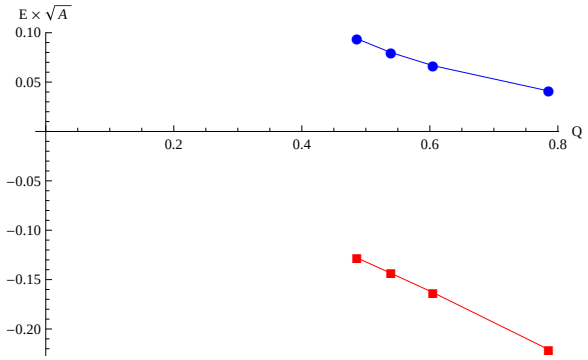

Figure 5.6: Graph of the interior Casimir energy E for various plane figures, multiplied by the square-root of the area A. These are plotted as a function of the isoperimetric quotient, $\mathcal{Q} = 4\pi \times A/P^2$. The points shown are for the hemiequilateral triangle, the isosceles right triangle, the equilateral triangle, and the square. The upper curve shows the result for Dirichlet modes, the lower curve the energy for Neumann modes.

ratio b/a. It is then possible to write

$$\frac{b}{a} = \frac{4\pi - 8\mathcal{Q}}{32\pi\mathcal{Q}} - \frac{\sqrt{\pi^2 - 4\pi\mathcal{Q}}}{2\mathcal{Q}}\,, \tag{5.61}$$

where $\mathcal{Q} = 4\pi \times A/P^2$, the isoperimetric coefficient. $\mathcal{Q}$ takes on the maximum value of $\pi/4$ for a square. Ideally, we would expect the data points for rectangular polygons and cylinders to prolong the interesting behavior we have observed in Figs. 5.6 and 5.5, but what we observe is even more interesting. These curves, for all the boundary conditions considered, instead intersect at a point. In addition, it seems the triangles and rectangles, each follow a certain hierarchy. The equilateral triangle has the least energy for all the triangles, although it has the highest $\mathcal{Q}$, and the square has the highest energy amongst the rectangles while still having the highest isoperimetric

quotient. We hypothesize that polygons with the same number of sides, say n, will belong to the same curve. These curves will likely connect to a curve of maximal isoperimetric quotients at the data points for the corresponding regular n-gons.

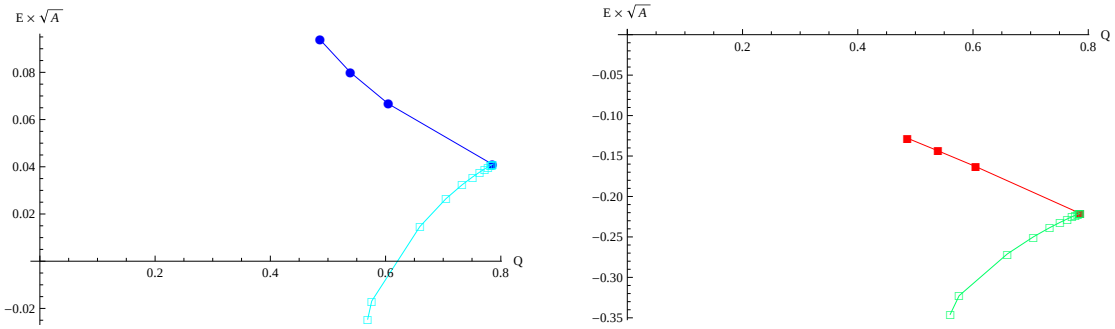

(a) Dirichlet BC

(b) Neumann BC

Figure 5.7: Graph of scaled Casimir energies for Dirichlet and Neumann polygons vs. $\mathcal{Q}$. $\mathcal{Q}$ is the isoperimetric quotient $4\pi \times A/P^2$. The upper curves connects the data points for the hemiequilateral, right isosceles, equilateral triangles and the square. The lower curves are for the rectangles. Note that they connect to the upper curves at the square's markers.

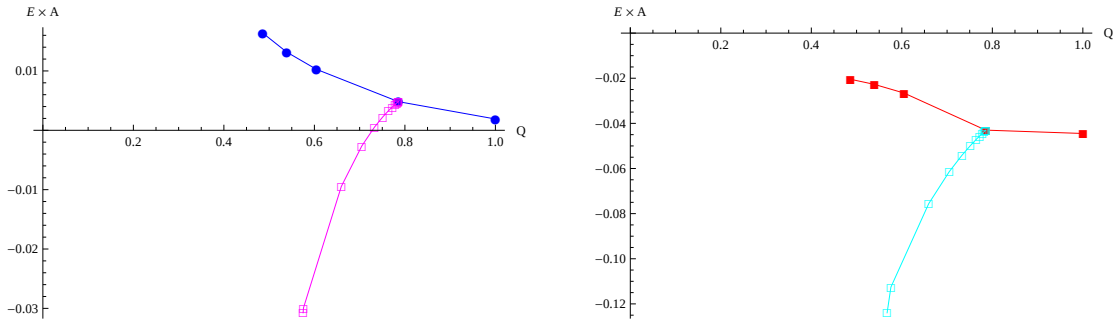

(a) Dirichlet BC

(b) Neumann BC

Figure 5.8: Graph of scaled Casimir energies, $\mathcal{E} \times A$, for Dirichlet and Neumann cylinders vs. $\mathcal{Q}$, the isoperimetric quotient. The markers for the integrable triangular, square, and circular cylinders are connected by the upper curves. The lower curves connects the markers for rectangular cylinders. The curves join at the markers corresponding to the square cylinders.

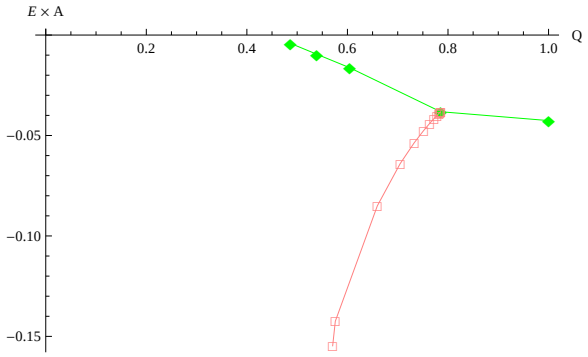

Figure 5.9: Graph of scaled Casimir energies for EM cylinders vs. $\mathcal{Q}$, the isoperimetric quotient. The lower curve, connecting data points for rectangular cylinders, joins the upper curve at the square's data point. The other markers on the upper curve, from left to right, are for the hemiequilateral, right isosceles, equilateral triangles, (the square), and the circular cylinder.

Chapter 6

Casimir Energies of Finite Prisms

In the previous chapter, we derived Casimir energies for integrable polygons and polygonal cylinders. Those were two extremes in height, the polygons are prisms of zero height and the infinite prisms, of course, have infinite height. How about the intermediate scenario where the height b is finite and in between those extremes, $0 < b < \infty$?

Indeed, one can obtain finite prisms that are integrable by simply choosing the cross sections to be the previously mentioned integrable polygons. From these, one can recover the infinite cylinder results as limits of the finite prisms(See Ref. [23]). The zero height limit also reproduces Casimir's parallel plate result [23]. To build these finite prisms, the caps at the ends must form dihedral angles of $\pi/2$ with the other intersecting planes. What this implies, is that the eigenfunctions and eigenvalues for these new prisms are already known. All one has to do is to update the eigenvalues and eigenfunctions in the previous chapter to reflect the newer quantization in the third dimension, which we will label z. For prisms of height b, the Dirichlet eigenfunctions would be of the form:

$$\Phi_{\mathbf{m}}(\mathbf{r}) = [\Phi_{\mathbf{m}}(\mathbf{r}_\perp)] \sin\left(\frac{\pi k}{b} z\right) , \tag{6.1}$$

where $[\Phi_{\mathbf{m}}(\mathbf{r}_\perp)]$ are the modes given in Chapter 5. The Neumann characteristic functions will also follow suit with:

$$\Psi_{\mathbf{m}}(\mathbf{r}) = [\Psi_{\mathbf{m}}(\mathbf{r}_\perp)] \cos\left(\frac{\pi k}{b} z\right) . \tag{6.2}$$

As for the characteristic values, we simply add another mode number k:

$$\lambda^2_{\mathbf{m}} = \left[\lambda^2_{\mathbf{m}}\right] + \frac{\pi^2}{b^2}k^2\,. \tag{6.3}$$

The expressions in the square brackets are the eigenvalues for the corresponding integrable polygons, given in Chapter 5. The similarities do not end there; they extend even to the completeness constraints and the degeneracies. For the completeness constraints we add the conditions $k > 0$ and $k \geq 0$, respectively for Dirichlet and Neumann boundaries, to those of the polygons. As in all the Neumann cases covered so far, the origin $k = m = n = 0$ must be removed. The number of degeneracies is simply doubled. The sets of mode numbers which yield unphysical modes are obtained by appending $k = 0$ to the previous ones. The results given in this chapter are obtained by point-splitting regularization.

6.1 Equilateral Triangular Prism

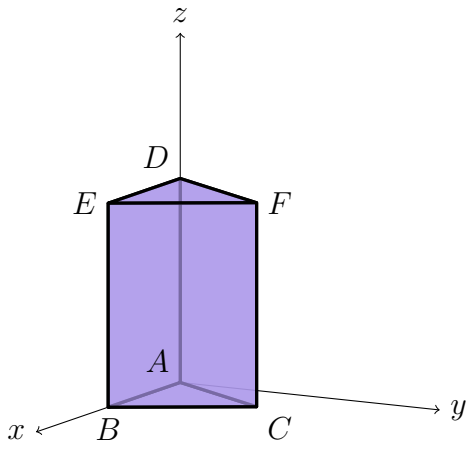

Figure 6.1: Equilateral prism. $|DE| = |EF| = |FD| = a$, and $|BE| = b$.

6.1.1 Dirichlet BC

Let g be the function defined by

$$g(r,s,k) = e^{-\tau\sqrt{\lambda_{\mathbf{m}}^2}}\,, \tag{6.4}$$

where the eigenvalues are written the diagonalized form (5.16):

$$\lambda_{\mathbf{m}}^2 = \frac{16\pi^2}{9a^2}(3\,r^2+s^2) + \frac{\pi^2}{b^2}k^2\,. \tag{6.5}$$

The mode numbers r and s can be integers as well as half-integers, whereas k can only be an integer. After symmetrically extending the sums, we obtain the energy,

$$E_{\rm EqP}^{(D)} = \frac{1}{24}\lim_{\tau\to 0}\left(-\frac{d}{d\tau}\right)\sum_{r,s,k=-\infty}^{\infty}\Big[g(r,s,k)+g(r+1/2,s+1/2,k) \tag{6.6}$$
$$-\,3\,g(0,s,k)-g(r,s,0)+3\,g(0,s,0)+2\,g(0,0,k)\Big]\,.$$

In the expression above, the mode numbers are all integers and we follow the same convention, described in the previous chapter, regarding the significance of the arguments being null. Applying the appropriate regularization formulæ, we write the Casimir energy, in terms of $\chi \equiv (b/a)^2$:

$$E_{\rm EqP}^{(D)} = \frac{1}{a}\Bigg\{-\frac{\sqrt{3\chi}}{\pi^2}\big[Z_3(2;3,9,16\chi)+Z_{3c}(2;3,9,16\chi)\big]+\frac{5}{48\pi}\zeta(3/2)L_{-3}(3/2) \tag{6.7}$$
$$+\frac{1}{24\pi}Z_{2b}(3/2;1,3)+\frac{3\sqrt{\chi}}{2\pi}Z_2(3/2;9,16\chi)-\frac{\pi}{36}-\frac{\pi}{72\sqrt{\chi}}\Bigg\},$$

where we used [37]

$$\sum_{m,n=-\infty}^{\infty}{}' (m^2+3n^2)^{-s} = 2(1+2^{1-2s})\,\zeta(s)L_{-3}(s)\,. \tag{6.8}$$

The Epstein zeta functions Z_3, Z_{3c}, etc. are defined in Appendix A. This particular configuration was considered earlier by Ahmedov and Duru [47], although their result appears misleading.

6.1.2 Neumann BC

After following the same approach and further simplifications, we can relate the Neumann result to the Dirichlet result,

$$E_{\mathrm{EqP}}^{(N)} = E_{\mathrm{EqP}}^{(D)} - \frac{1}{24\pi a}\Big[5\,\zeta(3/2)L_{-3}(3/2) + 2\,Z_{2b}(3/2;1,3) + 72\sqrt{\chi}\;Z_2(3/2;9,16\chi)\Big]\,. \tag{6.9}$$

6.2 Hemiequilateral Triangular Prism

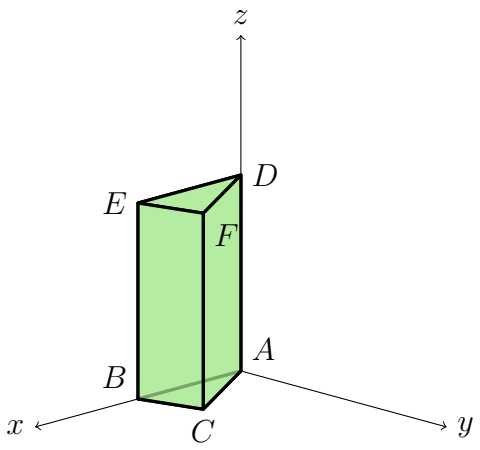

Figure 6.2: Hemiequilateral prism. $|DF| = a\sqrt{3/4}$, $|EF| = a/2$, $|DE| = a$, and $|BE| = b$.

6.2.1 Dirichlet BC

The spectrum for the hemiequilateral prism of finite height b is of the same form as the equilateral's (6.5). Again, in terms of $\chi \equiv (b/a)^2$, we find that the Dirichlet Casimir energy is of the form

$$E^{(D)}_{\mathrm{HemP}} = \frac{1}{2}E^{(D)}_{\mathrm{EqP}} + \frac{\sqrt{3\chi}}{4\pi a}Z_2(3/2;3,16\chi) - \frac{\pi}{72a}\Big(\sqrt{3}+\frac{3}{4\sqrt{\chi}}\Big). \tag{6.10}$$

6.2.2 Neumann BC

In relation to the previous result, we write

$$E^{(N)}_{\mathrm{HemP}} = \frac{1}{2}E^{(N)}_{\mathrm{EqP}} - \frac{\sqrt{3\chi}}{4\pi a}Z_2(3/2;3,16\chi) - \frac{\pi}{72a}\Big(\sqrt{3}+\frac{3}{4\sqrt{\chi}}\Big)\,. \tag{6.11}$$

6.3 Cube

6.3.1 Dirichlet BC

The Dirichlet Casimir energy for a cube of edge length a is simply

$$E^{(D)}_{\mathrm{Cube}} = \frac{1}{a}\bigg[-\frac{1}{32\pi^2}\,Z_3(2;1,1,1) + \frac{3}{16\pi}\,\zeta(3/2)\beta(3/2) - \frac{\pi}{32}\bigg]\,, \tag{6.12}$$

from which we obtain the finite part, a result which matches that of Ref. [19]:

$$E^{(D)}_{\mathrm{Cube}} = -\frac{0.0157321825}{a}\,. \tag{6.13}$$

6.3.2 Neumann BC

The Neumann result can be related to the Dirichlet result with

$$E^{(N)}_{\mathrm{Cube}} = E^{(D)}_{\mathrm{Cube}} - \frac{3}{8\pi a}\zeta(3/2)\beta(3/2), \tag{6.14}$$

which gives a numerical value already confirmed in Ref. [19]:

$$E^{(N)}_{\text{Cube}} = -\frac{0.2853094722}{a}. \tag{6.15}$$

6.4 Right Isosceles Triangular Prism

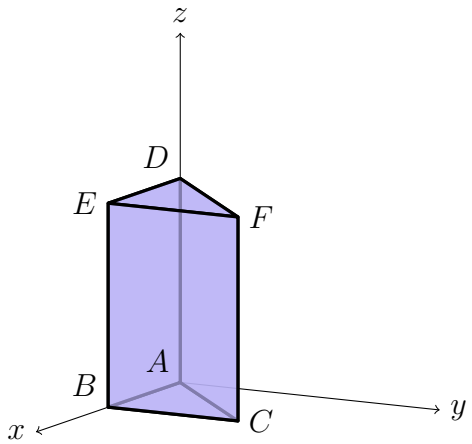

Figure 6.3: Right isosceles prism. $|DE| = |EF| = a$, $|DF| = a\sqrt{2}$, and $|BE| = b$.

6.4.1 Dirichlet BC

Just like the previous prisms, the spectrum and other relevant information for the right isosceles triangular prism of finite height can be inferred from the details furnished in the previous chapter. From these, we deduce that the Casimir energy, in terms of $\chi \equiv (b/a)^2$, is:

$$E^{(D)}_{\text{RIsoP}} = \frac{1}{a}\Bigg[-\frac{\sqrt{\chi}}{64\pi^2} Z_3(2;1,1,\chi) + \frac{1}{32\pi}\zeta(3/2)\beta(3/2) + \frac{\sqrt{\chi}}{64\pi} Z_2(3/2;1,\chi) \\ + \frac{\sqrt{\chi}}{32\pi} Z_2(3/2;1,2\chi) - \frac{\pi}{64\sqrt{\chi}} - \frac{\pi(1+\sqrt{2})}{96}\Bigg]. \tag{6.16}$$

When $\chi = 1$, which makes that particular prism a section of a cube with edge length a, we can write:

$$E^{(D)}_{\text{RIsoP}} = \frac{1}{2} E^{(D)}_{\text{Cube}} + \frac{1}{96\pi a}\left[3\,\zeta(3/2) L_{-8}(3/2) - \pi^2\left(1+\sqrt{2}\right)\right]. \tag{6.17}$$

6.4.2 Neumann BC

In terms of the Dirichlet result, we find:

$$E^{(N)}_{\text{RIsoP}} = E^{(D)}_{\text{RIsoP}} - \frac{1}{32\pi a}\Big[2\,\zeta(3/2)\beta(3/2) + \sqrt{\chi}\, Z_2(3/2;1,\chi) + 2\sqrt{\chi}\, Z_2(3/2;1,2\chi)\Big]. \tag{6.18}$$

Likewise, when $\chi = 1$, we can relate the energy to a cube of corresponding edge length a:

$$E^{(N)}_{\text{RIsoP}} = \frac{1}{2} E^{(N)}_{\text{Cube}} - \frac{1}{96\pi a}\left[3\,\zeta(3/2) L_{-8}(3/2) + \pi^2\left(1+\sqrt{2}\right)\right]. \tag{6.19}$$

6.5 Rectangular Parallelepipeds

6.5.1 Dirichlet BC

The cube is a specific element of the class of rectangular parallelepipeds, much like the square belongs to the set of rectangles. Just like the previous cases, the Casimir energy may be written in terms of Epstein zeta functions and the ratios $\chi \equiv (b/a)^2$ and $\sigma \equiv (c/a)^2$:

$$E^{(D)}_P = \frac{1}{a}\Bigg\{ -\frac{\sqrt{\chi\,\sigma}}{32\pi^2}\, Z_3(2;1,\chi,\sigma) + \frac{1}{64\pi}\Big[\sqrt{\chi\,\sigma}\, Z_2(3/2;\chi,\sigma) + \sqrt{\sigma}\, Z_2(3/2;1,\sigma) + \sqrt{\chi}\, Z_2(3/2;1,\chi)\Big] - \frac{\pi}{96}\Big(1 + \frac{1}{\sqrt{\chi}} + \frac{1}{\sqrt{\sigma}}\Big)\Bigg\}. \tag{6.20}$$

6.5.2 Neumann BC

In terms of the Dirichlet result we obtain

$$E_P^{(N)} = E_P^{(D)} - \frac{1}{32\pi a}\Big[\sqrt{\chi\,\sigma}\,Z_2(3/2;\chi,\sigma) + \sqrt{\sigma}\,Z_2(3/2;1,\sigma) + \sqrt{\chi}\,Z_2(3/2;1,\chi)\Big]\,. \tag{6.21}$$

When $\sigma = 1$, we will refer to this configuration as a *square prism*. If both σ and χ are equal to one, then we recognize this geometry as the cube.

6.6 Analysis

Now that we have calculated scalar Casimir energies for finite prisms (Dirichlet and Neumann boundary conditions), we can proceed with the analysis just like the ones for the infinite prisms and polygons. Likewise, we begin by finding an objective way to relate these energies to their geometries. Since these finite prisms are polyhedra, we must employ the isoareal quotient, which we introduced in Chapter 4 earlier (4.17),

$$\mathcal{Q} = 36\pi\,\frac{V^2}{S^3}\,. \tag{6.22}$$

The energies must also be scaled in order to be rid of the explicit dependence on the system's size. For the polygons and infinite prisms we simply multiplied the energies by the cross-sectional area or its square-root as needed. Here, however, the scale factor is a combination of two geometrical properties V/S, the ratio of the volume to the surface area. We define the scaled energy for a polyhedron as,

$$E_{sc} = E\,\frac{V}{S}\,. \tag{6.23}$$

Cross section	$E_{sc}^{(D)}$	$E_{sc}^{(N)}$	$\mathcal{Q}_{\max}$
Hemiequilateral Tr.	-0.004483	-0.034166	0.324004
Isosceles Right Tr.	-0.004028	-0.035478	0.359341
Equilateral Tr.	-0.003571	-0.037783	0.403067
Square	-0.002622	-0.0475552	0.523599

Table 6.1: Scaled Casimir energies for finite prisms having maximal isoareal quotients $\mathcal{Q}_{\max}$. The second and third column from the left give, respectfully, the scaled Dirichlet and Neumann energies. Of note, the square prism (rectangular parallelepiped with $\sigma = 1$) having maximal $\mathcal{Q}$ is none other than the cube.

Listed in Table 6.1 are the scaled energies for the finite prisms having the maximal isoareal quotients of their categories. In other words, these energies are for the finite prisms that have the maximal isoareal quotients for a specific choice of edge lengths a and b. We plot the information given in Table 6.1 in Figs. 6.4a and 6.4b, to find an interesting hierarchy. It appears, the triangular prisms of maximal $\mathcal{Q}$ tend to line up, in the same order as the infinite prisms and polygons. However, they differ in subtle ways: the Dirichlet energies are now increasing instead of decreasing, for example. For the triangular polygons and their infinite counterparts, the equilateral triangle had the minimal scaled energy. For the finite triangular prisms having $\mathcal{Q}_{max}$, the equilateral triangle has the maximal scaled energy. The cube, which is the square prism of maximal $\mathcal{Q}$, also follows directly after the equilateral triangular prism's data

point, thus continuing the apparent ascension. Later, in a more inclusive analysis, we will show that this apparent ascension may be more than apparent when we include the results for a spherical shell.

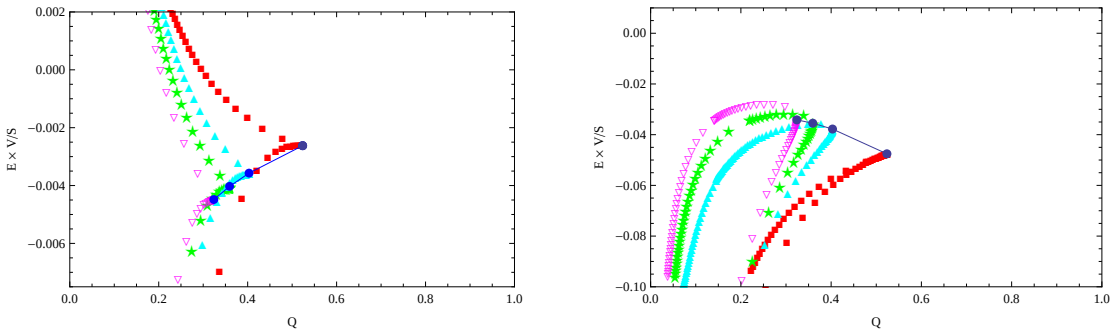

(a) Dirichlet BC

(b) Neumann BC

Figure 6.4: The scaled energies for Dirichlet (left) and Neumann (right) finite prisms are plotted against the isoareal quotients $\mathcal{Q}$. From left to right, the plotted curves are for the hemiequilateral, right isosceles, equilateral triangular prisms, and the square prims. The circular markers indicate the particular configurations having the maximal Q for each cross section.

What we are observing in these plots and data begins to reinforce the idea that these energies, at least, follow certain hierarchies within a chosen class of geometries. It seems plausible that we could have different branches for different geometry classes which are then inter-related by the relations of their respective elements having the highest $\mathcal{Q}$.

When we pay closer attention to Figs. 6.4a and 6.4b, we also notice that for the same value of $\mathcal{Q}$, there can be two corresponding energies. This could mean

that in order to specify a unique configuration, we need more that just the isoareal quotient. We do know that the scaled energies for finite prisms do depend on the ratio $\chi \equiv (b/a)^2$. Would plotting scaled energies with respect to $\mathcal{Q}$ and χ or some other geometric invariant display patterns of interest? One geometric invariant related to χ is b^2/A, the ratio of the square of the height to the cross-sectional area. Plotting $\mathcal{Q}$ against these two variables in Figs. 6.5a and 6.5b, we see that $\mathcal{Q}$ has a smoother dependence on the b^2/A. Hence, we choose to plot the scaled energies E_{sc} against $\mathcal{Q}$ and b^2/A in Fig. 6.6. It seems, though, that not much information can be gathered in the previously mentioned plot that is not already displayed in the other plots.

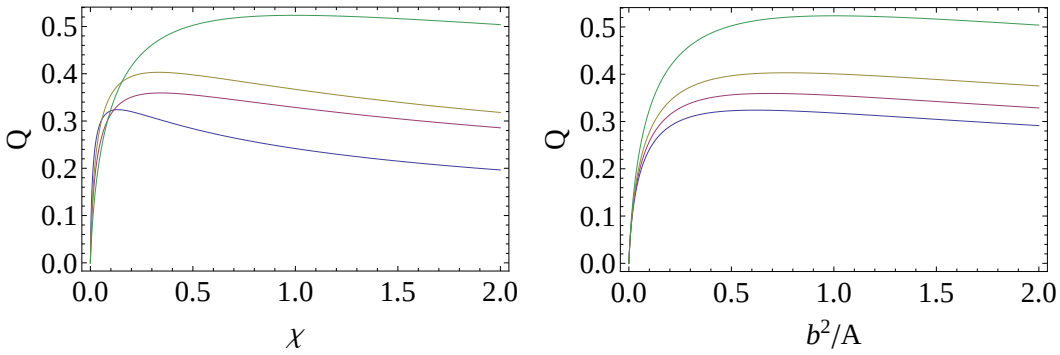

(a) (b)

Figure 6.5: In the left figure, the isoareal quotients $\mathcal{Q}$ are plotted against $\chi = (b/a)^2$. To the right, the isoareal quotients are plotted against the geometric invariant b^2/A (A is the cross-sectional area). From bottom to top, the curves correspond to the hemiequilateral, right isosceles, equilateral finite triangular prisms, and the square prism.

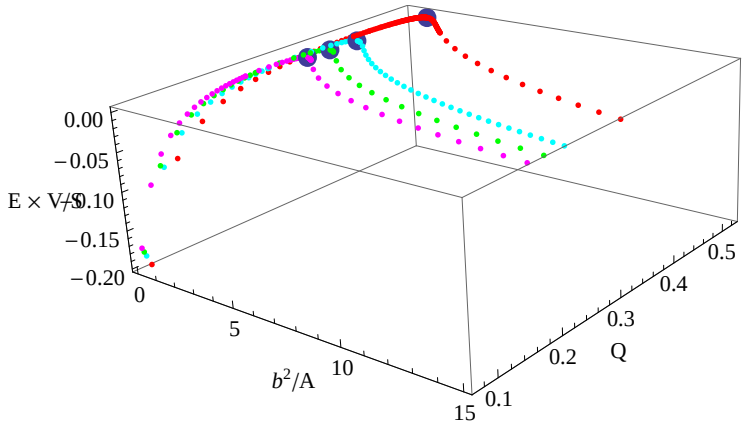

Figure 6.6: Scaled Dirichlet energies of prisms vs. isoareal quotients $\mathcal{Q}$ and b^2/A, where A is the cross-sectional area. Starting from the lowest $\mathcal{Q}$-values, the curves correspond respectively to hemiequilateral, right isosceles, and equilateral triangular prisms, and square prisms (parallelepipeds with $\sigma = 1$). The prominent circular markers are for the configurations having the maximal $\mathcal{Q}$.

Chapter 7

Casimir Energies of Tetrahedra

In Chapter 4, we listed all the polyhedral cavities for which the method of images applies. So far, we have looked at almost every case except the three integrable tetrahedra. The eigenfunctions and eigenvalues for these tetrahedral domains can be obtained using the straightforward approach described in the latter chapter. In fact, they are not recent discoveries. The information about the eigenvalues and eigenfunctions for such tetrahedra is present in a few articles [40, 62, 63]. The Casimir energy results we give in this section are new. There appears to be only one earlier Casimir energy treatment for one of these tetrahedra, which we denote here as the *small tetrahedron*. That result, however, is erroneous. We will successively look at the *large*, *medium*, and *small tetrahedra*, as defined below, and obtain interior scalar Casimir energies for Dirichlet and Neumann boundary conditions.

7.1 Large Tetrahedron

We label the most symmetrical of these tetrahedra, sketched in Fig 7.1, as *large*. Comparatively it seems to be the largest, since one can obtain a medium tetrahedron by halving a large tetrahedron and idem for a small and medium tetrahedron. These terms, *large*, *medium*, and *small*, are merely labels since one can always rescale each tetrahedron independently of the others. Therefore, one should be careful not to ascribe much meaning to these labels. The eigenvalues for a large tetrahedron are of

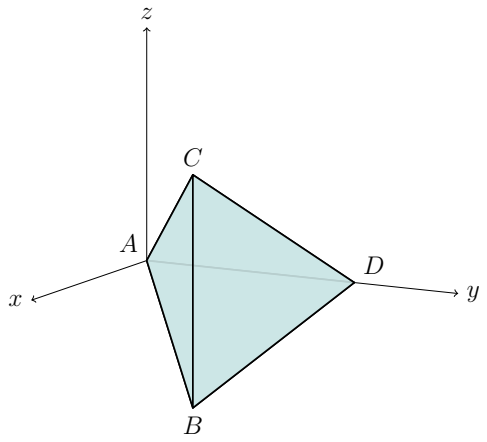

Figure 7.1: Large tetrahedron: $-x < z < x$ and $x < y < 2a - x$.

the form:

$$\lambda_{\mathbf{m}}^2 = \frac{\pi^2}{4a^2}\left[3(k^2+m^2+n^2) - 2(km+kn+mn)\right] , \tag{7.1}$$

where k, m, n are integers.

7.1.1 Dirichlet BC

The Dirichlet eigenfunctions for a large tetrahedron, bounded by the planes $z = x$, $z = -x$, $y = x$, and $y = 2a - x$, take the form (after simplifications) [40]:

$$\Phi_{\mathbf{m}}(\mathbf{r}) = \alpha_{\mathbf{m}}(\mathbf{r}) - i\,\beta_{\mathbf{m}}(\mathbf{r}) \tag{7.2}$$

where we write succinctly,

$$\alpha_{\mathbf{m}}(\mathbf{r}) = \begin{vmatrix} \cos(\pi p\, x/2a) & \cos(\pi p\, y/2a) & \cos(\pi p\, z/2a) \\ \cos(\pi q\, x/2a) & \cos(\pi q\, y/2a) & \cos(\pi q\, z/2a) \\ \cos(\pi r\, x/2a) & \cos(\pi r\, y/2a) & \cos(\pi r\, z/2a) \end{vmatrix} \tag{7.3}$$

and

$$\beta_{\mathbf{m}}(\mathbf{r}) = \begin{vmatrix} \sin(\pi p\, x/2a) & \sin(\pi p\, y/2a) & \sin(\pi p\, z/2a) \\ \sin(\pi q\, x/2a) & \sin(\pi q\, y/2a) & \sin(\pi q\, z/2a) \\ \sin(\pi r\, x/2a) & \sin(\pi r\, y/2a) & \sin(\pi r\, z/2a) \end{vmatrix} . \tag{7.4}$$

For simplicity, the variables p, q, and r are actually defined in terms of the mode numbers: $p = k + m - n$, $q = k - m + n$, and $r = -k + m + n$. $\alpha_{\mathbf{m}}$ and $\beta_{\mathbf{m}}$, together, form the set of all possible eigenfunctions. To form a complete set, we must constrain the mode numbers to $0 < n < m < k$. To symmetrically extend these constrained sums over all possible values, we need to remove all the unphysical cases, and account for the degeneracies. We can check that the modes (7.3) and (7.4) are degenerate for 24 operations on the x,y,z coordinates and that all the unphysical cases correspond to $\{k = 0, m = 0, n = 0, k = m, k = n, m = n\}$. Using this information and the function

$$g(p, q, r) = e^{-\tau\sqrt{(\pi/a)^2(p^2+q^2+r^2)}}\,, \tag{7.5}$$

the unregularized Casimir energy is of the form

$$\begin{aligned} E = \frac{1}{48} \lim_{\tau\to 0} \left(-\frac{d}{d\tau}\right) \sum_{p,q,r=-\infty}^{\infty} \Big[& g(p,q,r) + g(p+1/2, q+1/2, r+1/2) \\ & - 6\, g(p,q,q) - 6\, g(p+1/2, q+1/2, q+1/2) \\ & + 8\, g(\sqrt{3}p/2, 0, 0) + 3\, g(p, 0, 0) \Big] . \end{aligned} \tag{7.6}$$

The sums extend over all positive and negative integers including zero. (In the third and fourth terms only p and q are summed over, while in the last two terms only p is summed.) We then extract the finite part using the regularization formulæ in Eqs. (3.5), (3.6), and (3.7). The Epstein zeta functions Z_3, Z_{3b}, etc. are defined in

Appendix B,

$$E_L^{(D)} = \frac{1}{a}\Bigg\{ -\frac{1}{96\pi^2}\big[Z_3(2;1,1,1) + Z_{3b}(2;1,1,1)\big] + \frac{1}{8\pi}\zeta(3/2)L_{-8}(3/2) + \frac{1}{16\pi}Z_{2b}(3/2;2,1) - \frac{\pi}{96} - \frac{\pi\sqrt{3}}{72}\Bigg\}, \tag{7.7}$$

where (the prime means the origin is excluded) [37]

$$\sum_{m,n=-\infty}^{\infty}{}' (m^2+2n^2)^{-s} = 2\zeta(s)L_{-8}(s)\,. \tag{7.8}$$

The energy then evaluates numerically to

$$E_L^{(D)} = -\frac{0.0468804266}{a}\,. \tag{7.9}$$

The divergent parts, also extracted from the regularization procedure, follow the expected form of Weyl's law (3.11)

$$E_{\rm div}^{(D)} = \frac{3V}{2\pi^2\tau^4} - \frac{S}{8\pi\tau^3} + \frac{C}{48\pi\tau^2}\,. \tag{7.10}$$

7.1.2 Neumann BC

The Neumann modes are similar to the Dirichlet ones, except they are a symmetric sum instead of an antisymmetric sum. We have

$$\Psi_{\mathbf{m}}(\mathbf{r}) = \gamma_{\mathbf{m}}(\mathbf{r}) - i\,\delta_{\mathbf{m}}(\mathbf{r})\,, \tag{7.11}$$

where $\gamma_{\mathbf{m}}$ is the symmetric sum version of $\alpha_{\mathbf{m}}$ (7.3), and $\delta_{\mathbf{m}}$ has the same relation to $\beta_{\mathbf{m}}$ (7.4). The completeness constraints are $0 \le n \le m \le k$ excluding the origin $k = m = n = 0$. After regularizing the resulting expression, we can simplify the expression in terms of the Dirichlet result:

$$E_L^{(N)} = E_L^{(D)} - \frac{1}{8\pi a}\Big[2\,\zeta(3/2)L_{-8}(3/2) + Z_{2b}(3/2;2,1)\Big], \tag{7.12}$$

which gives us a numerical value of

$$E_L^{(N)} = -\frac{0.1964621484}{a}\,. \tag{7.13}$$

The divergent parts also match the expected Weyl terms for Neumann boundary conditions.

7.2 Medium Tetrahedron

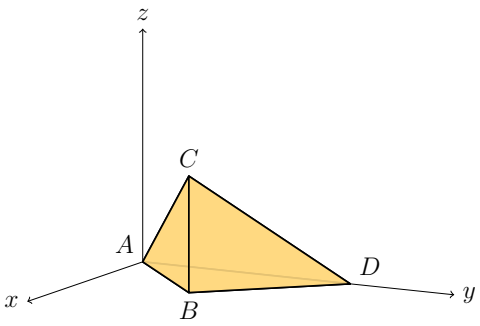

Figure 7.2: Medium tetrahedron: $0 < z < x$ and $x < y < 2a - x$.

The medium tetrahedron, sketched in Fig. 7.2, can be obtained by halving the large tetrahedron in Fig. 7.1 across the $z = 0$ plane. The eigenvalue spectra are of the same form (7.1), but the constraints are obviously not.

7.2.1 Dirichlet BC

The Dirichlet modes for a medium tetrahedron [40] with the specifications given in Fig. 7.2 are a subset of the large tetrahedron's (7.4):

$$\Phi_{\mathbf{m}}(\mathbf{r}) = \begin{vmatrix} \sin(\pi p\, x/2a) & \sin(\pi p\, y/2a) & \sin(\pi p\, z/2a) \\ \sin(\pi q\, x/2a) & \sin(\pi q\, y/2a) & \sin(\pi q\, z/2a) \\ \sin(\pi r\, x/2a) & \sin(\pi r\, y/2a) & \sin(\pi r\, z/2a) \end{vmatrix} . \tag{7.14}$$

These are, in fact, the modes for the large tetrahedron that vanish for $z = 0$. p, q, and r have the same definitions in terms of the integers k, m, n given in Section 7.1.1. The completeness constraints are $n < m < k < m+n$. This time there are 48 degeneracies, and the unphysical modes have the mode numbers $\{k = 0, m = 0, n = 0, k = m, k = n, m = n, k = m + n, m = k + n, n = k + m\}$. The energy, in terms of the large tetrahedron's result, is

$$E_M^{(D)} = \frac{1}{2}\, E_L^{(D)} + \frac{1}{96\pi a}\Big[3\,\zeta(3/2)\beta(3/2) - (1+\sqrt{2})\pi^2\Big], \tag{7.15}$$

where we used [37]

$$\sum_{m,n=-\infty}^{\infty}{}' \,(m^2+n^2)^{-s} = 4\zeta(s)\beta(s)\,. \tag{7.16}$$

The Casimir energy evaluates to

$$E_M^{(D)} = -\frac{0.0799803933}{a}\,. \tag{7.17}$$

Here the function β is also defined in Appendix B.

7.2.2 Neumann BC

The Neumann modes are also a subset of the large tetrahedron's (Neumann modes). They are labeled as $\delta_{\mathbf{m}}$ in the previous section. The constraints for the complete set of modes is also a more inclusive version of the Dirichlet constraint: $n \leq m \leq k \leq m+n$, which still excludes the origin $k = m = n = 0$. We express this result in terms of the large tetrahedron's energy (7.13):

$$\begin{aligned} E_M^{(N)} &= \frac{1}{2}\, E_L^{(N)} - \frac{1}{96\pi a}\Big[3\,\zeta(3/2)\beta(3/2) + (1+\sqrt{2})\pi^2\Big] \\ &= -\frac{0.1997008024}{a}\,. \end{aligned} \tag{7.18}$$

7.3 Small Tetrahedron

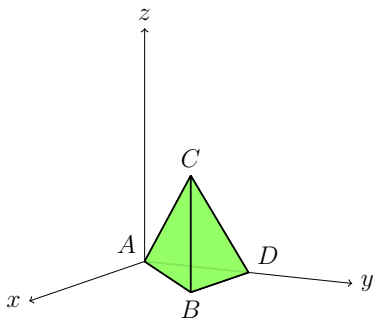

Figure 7.3: Small tetrahedron: $0 < z < x$ and $x < y < a$.

The small tetrahedron in Fig. 7.3 can be thought of as the result of dividing the medium tetrahedron (Fig. 7.1) across the $y = a$ plane. The eigenvalues, this time, however, are of a different form

$$\lambda_{\mathbf{m}}^2 = \frac{\pi^2}{a^2}\left(k^2 + m^2 + n^2\right)\,. \tag{7.19}$$

They are actually of the same form as a cube's eigenvalue spectrum[1], although as we expect they have different modal constraints.

7.3.1 Dirichlet BC

For Dirichlet boundary conditions, the modes are similar to $\beta_{\mathbf{m}}$ in Eq. (7.4),

$$\Phi_{\mathbf{m}}(\mathbf{r}) = \begin{vmatrix} \sin(\pi k\, x/a) & \sin(\pi k\, y/a) & \sin(\pi k\, z/a) \\ \sin(\pi m\, x/a) & \sin(\pi m\, y/a) & \sin(\pi m\, z/a) \\ \sin(\pi n\, x/a) & \sin(\pi n\, y/a) & \sin(\pi n\, z/a) \end{vmatrix}, \tag{7.20}$$

but here the sines are functions of k, m, and n, which are integers, not combinations of integers. To specify a complete set of modes, we must have $0 < n < m < k$. To obtain the zero-point energy, we proceed with our method of symmetrical extension, where we remove the unphysical cases $\{k = 0, m = 0, n = 0, k = \pm m, k = \pm n, m = \pm n\}$ and account for the 48 degeneracies. The finite part obtained is thus

$$E_S^{(D)} = \frac{1}{a}\Bigg[-\frac{1}{192\pi^2} Z_3(2;1,1,1) + \frac{1}{16\pi}\zeta(3/2)L_{-8}(3/2) + \frac{1}{32\pi}\zeta(3/2)\beta(3/2) - \frac{\pi}{64} - \frac{\pi\sqrt{3}}{72} - \frac{\pi\sqrt{2}}{96}\Bigg], \tag{7.21}$$

which evaluates to

$$E_S^{(D)} = -\frac{0.10054146218}{a}\,. \tag{7.22}$$

This particular configuration was considered in Ref. [46], where it was called a *pyramidal cavity*. The result given in that reference, however, is likely wrong and the issue appears to stem from a mode-counting error.

[1] This spectrum is actually the same as that for the other tetrahedra, given in Eq. (7.1), with the additional restriction that $m + n + k$ be even.

7.3.2 Neumann BC

For Neumann boundaries, the treatment is just as straightforward. The modes are also of the same form as the medium tetrahedron's, which we give explicitly:

$$\begin{aligned}\Psi_{\mathbf{m}}(\mathbf{r}) = \cos(\pi kx/a)\big[\cos(\pi my/a)\cos(\pi nz/a) + \cos(\pi ny/a)\cos(\pi nz/a)\big] \\ + \cos(\pi mx/a)\big[\cos(\pi ky/a)\cos(\pi nz/a) + \cos(\pi ny/a)\cos(\pi kz/a)\big] \\ + \cos(\pi nx/a)\big[\cos(\pi my/a)\cos(\pi kz/a) + \cos(\pi ky/a)\cos(\pi mz/a)\big]\,.\end{aligned} \tag{7.23}$$

Again, $k, m, n \in \mathbb{Z}$. We symmetrically extend the sums, which are constrained by $0 \le n \le m \le k$ minus the origin $k = m = n = 0$, and we obtain the energy

$$E_S^{(N)} = E_S^{(D)} - \frac{1}{16\pi a}\zeta(3/2)\Big[2\,L_{-8}(3/2) + \beta(3/2)\Big], \tag{7.24}$$

in terms of $E_S^{(D)}$ (7.22). This gives a numerical value of

$$E_S^{(N)} = -\frac{0.2587920021}{a}\,. \tag{7.25}$$

7.4 Analysis

To try to make sense of, or rather discover the underlying mechanism responsible for the geometry-energy conundrum we will plot the scaled energies of the tetrahedra with respect to their isoareal quotients $\mathcal{Q}$. Both quantities have been introduced in the previous analyses for the finite prisms in Section 6.6. We compile the data for these scaled energies and isoareal quotients in Table 7.1, and later plot them in Figs. 7.4a, 7.4b, 7.5a, and 7.5b.

At this stage, it is quite unclear what the nature of these curves are, like all the other geometries analyzed so far. These curves, for the tetrahedra, do not display the monotonic behavior observed for the prisms, for example. Although this may be counter-intuitive, one must be open to the various possibilities presented. In fact, three data points may not be enough to capture the salient characteristics of a curve. Furthermore, how does this fit with the systematics we have already observed?

Cavity	$\mathcal{Q}$	$E_{\mathrm{sc}}^{(D)}$	$E_{\mathrm{sc}}^{(N)}$
Small T.	0.22327	-0.00694	-0.01787
Medium T.	0.22395	-0.00696	-0.01739
Large T.	0.27768	-0.00552	-0.02315
Cube	0.52359	-0.00262	-0.04755
Spherical Shell	1	0.00093	-0.07459

Table 7.1: Scaled energies and isoareal quotients. The last row is for a spherical shell. In contrast to the polyhedral results, which are only from interior contributions, the spherical shell's energies are the result of adding interior and exterior contributions [15, 64].

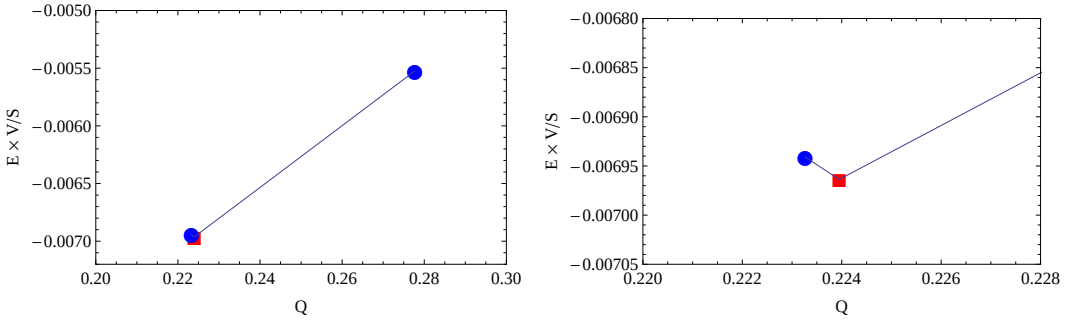

(a) (b)

Figure 7.4: Scaled energies of Dirichlet integrable tetrahedra vs. $\mathcal{Q}$. The figure on the left plots the energies for all three tetrahedra. In order of increasing Q, the plot markers correspond to the small, medium, and large tetrahedra. The figure on the right shows the relative positions of the small and medium tetrahedra's plot markers.

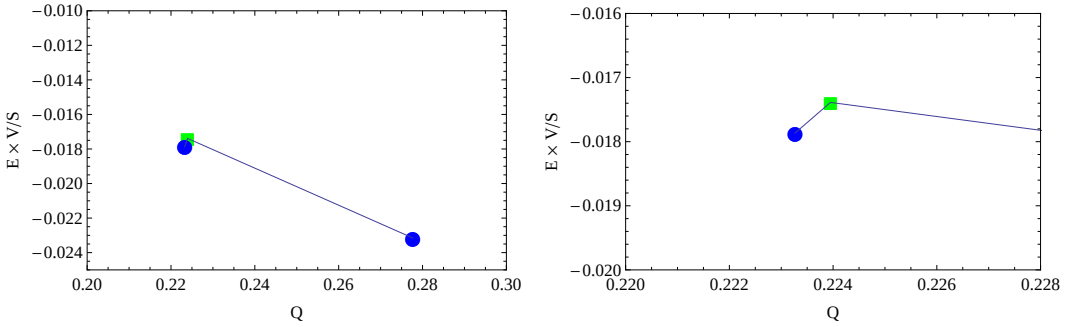

(a) (b)

Figure 7.5: Scaled energies of Neumann integrable tetrahedra vs. $\mathcal{Q}$. The figure on the left plots the energies for all three tetrahedra. In order of increasing Q, the plot markers correspond to the small, medium, and large tetrahedra. The figure on the right shows the relative positions of the small and medium tetrahedra's plot markers.

Chapter 8

Analysis and Conclusions

To recapitulate, the aim of this work is to seek a better understanding of the geometry-energy relation for the Casimir effect. In the past chapters, we derived and analyzed the Casimir energies for integrable cavities within their own categories. The question, though, remains about how the energies of vastly different geometries would compare.

Plotting the scaled energies for the finite prisms, tetrahedra, and spherical shell against their isoareal quotients on the same graph, we observe that there is an overall hierarchy for these clusters of data points. For example, in Fig. 8.1 where we consider Dirichlet boundaries, the tetrahedra have the lowest energies, followed by the finite prisms, and eventually the spherical shell. The order is reversed for Neumann boundaries (Fig. 8.2). These are interesting behaviors. There is, however, a concern regarding whether it is valid to compare the interior Casimir energies for polyhedra to a spherical shell's, which is obtained by adding both interior and exterior energies.

Although one cannot directly answer this question, the approach taken in this analysis is certainly a way to find a solution. Since the energies for polyhedral cavities are unambiguous (only the interior contributes), one would expect an interesting transition as the number of boundaries increases indefinitely to give a smooth boundary, for example a sphere. This would also allow one to assign an unambiguous interior energy for smooth boundaries, a problem which has often surfaced in bag model calculations.

Understanding self-energies is a fundamental problem which will certainly have

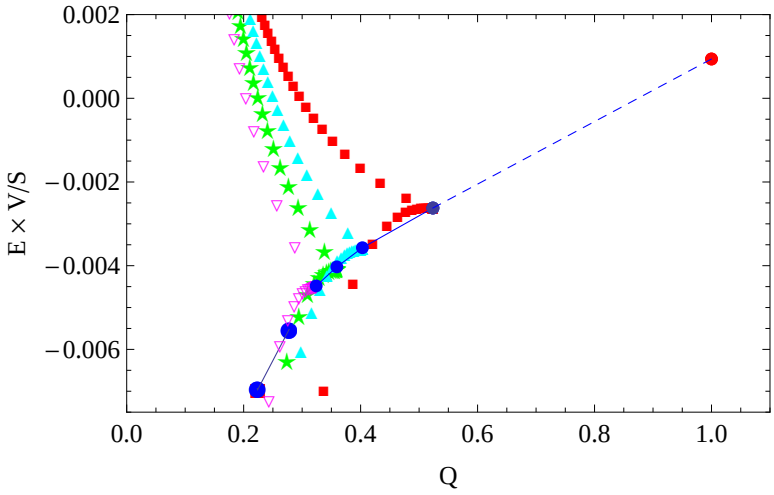

Figure 8.1: The scaled energies for Dirichlet integrable cavities (finite prisms, tetrahedra, including the spherical shell) are plotted against the isoareal quotients $\mathcal{Q}$. From left to right, we combine the plots for the tetrahedra (Fig. 7.4a), the finite prisms (Figs. 6.4a), and a red circular marker for a Dirichlet spherical shell (see Table 7.1).

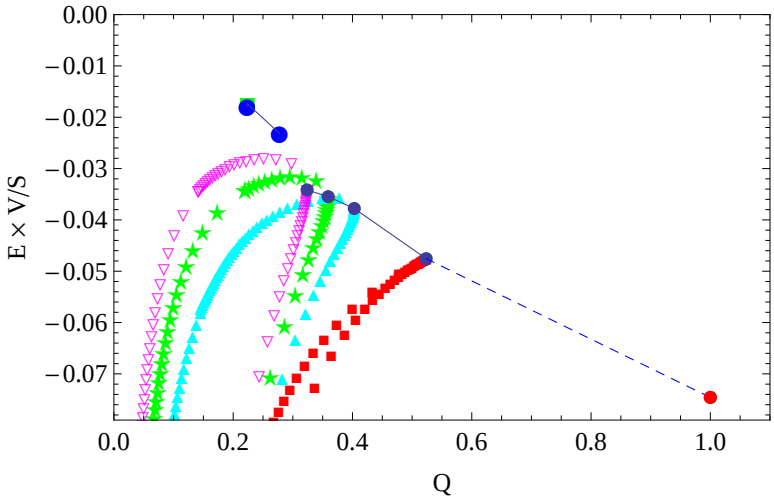

Figure 8.2: The scaled energies for Neumann integrable cavities (finite prisms, tetrahedra, including the spherical shell) are plotted against the isoareal quotients $\mathcal{Q}$. From left to right, we combine the plots for the tetrahedra (Fig. 7.5a), the finite prisms (Fig. 6.4b), and a red circular marker for a Neumann spherical shell (see Table 7.1).

positive repercussions. For instance, one could think of the dark energy problem in cosmology. Nanotechnology, where one is concerned with small scales, will also benefit from a better understanding of the Casimir effect. At the very least, the results obtained in this work are of mathematical significance. In the meantime, extending these results to other boundary conditions, notably electromagnetic boundary conditions, and higher dimensions is under way.

References

[1] H. B. G. Casimir, Physica **19**, 846 (1953).

[2] H. B. G. Casimir, Proc. Kon. Ned. Akad. Wetensch. **51**, 793 (1948).

[3] K. A. Milton, *The Casimir Effect* (World Scientific, New Jersey, 2001).

[4] M. J. Sparnaay, Physica **24**, 751 (1958).

[5] E. S. Sabisky and C. H. Anderson, Phys. Rev. A **7**, 790 (1973).

[6] S. K. Lamoreaux, Phys. Rev. Lett. **78**, 5 (1997).

[7] U. Mohideen and A. Roy, Phys. Rev. Lett. **81**, 4549 (1998).

[8] R. S. Decca, D. López, E. Fischbach, G. L. Klimchitskaya, D. E. Krause, and V. M. Mostepanenko, Ann. Phys. **318**, 37 (2005).

[9] T. H. Boyer, Phys. Rev. **174**, 1764 (1968).

[10] B. Davies, J. Math. Phys. **13**, 1324 (1972).

[11] R. Balian and B. Duplantier, Ann. Phys. **112**, 165 (1978).

[12] K. A. Milton, L. L. D. Jr., and J. Schwinger, Ann. Phys. **115**, 388 (1978).

[13] S. Leseduarte and A. Romeo, Ann. Phys. **250**, 448 (1996).

[14] S. Leseduarte and A. Romeo, Europhys. Lett. **34**, 79 (1996).

[15] V. V. Nesterenko and I. G. Pirozhenko, Phys. Rev. D **57**, 1284 (1998).

[16] W. Lukosz, Physica **56**, 109 (1971).

[17] W. Lukosz, Z. Phys. **262**, 327 (1973).

[18] W. Lukosz, Z. Phys. **258**, 99 (1973).

[19] J. Ambjørn and S. Wolfram, Ann. Phys. **147**, 1 (1983).

[20] L. L. DeRaad, Jr. and K. A. Milton, Ann. Phys. **136**, 229 (1981).

[21] E. K. Abalo, K. A. Milton, and L. Kaplan, Phys. Rev. D **82**, 125007 (2010).

[22] E. K. Abalo, K. A. Milton, and L. Kaplan, (2011), (To appear in IJMPCS Proceedings of QFEXT11).

[23] E. K. Abalo, K. A. Milton, and L. Kaplan, (2012), (Submitted to J. Phys. A).

[24] S. A. Fulling, J. Phys. A **36**, 6857 (2003).

[25] H. Weyl, Nachr. Königl. Gesell. Wiss. Göttingen 110 (1911).

[26] H. Weyl, Mathematische Annalen **71(4)**, 441 (1912).

[27] H. Weyl, J. Reine Angew. Math. **141**, 1 (1912).

[28] H. Weyl, J. Reine Angew. Math. **141**, 163 (1912).

[29] B. V. Fedosov, Sov. Math. Dokl. **4**, 1092 (1963).

[30] K. A. Milton and J. Schwinger, *Electromagnetic Radiation: Variational Methods, Waveguides and Accelerators* (Springer-Verlag, Berlin, 2006).

[31] E. Elizalde, S. D. Odintsov, A. Romeo, A. A. Bytsenko, and S. Zerbini, *Zeta Regularization Techniques with Applications* (World Scientific, Singapore, 1994).

[32] S. Chowla and A. Selberg, J. Reine Angew. Math. **227**, 86 (1967).

[33] L. Lorenz, Matematisk Tidsskrift **1**, 97 (1871).

[34] G. H. Hardy, Messenger Math. **49**, 85 (1919).

[35] A. Fletcher, J. C. P. Miller, L. Rosenhead, and L. J. Comrie, *An Index of Mathematical Tables* (Blackwell, London, 1962), Vol. 1, p. 95.

[36] I. J. Zucker, J. Math. Phys. **15**, 187 (1974).

[37] M. L. Glasser and I. J. Zucker, *Theoretical Chemistry: Advances and Perspectives* (Academic, New York, 1980).

[38] C. Itzykson, P. Moussa, and J. M. Luck, J. Phys. A **19**, L111 (1986).

[39] C. Itzykson and J. M. Luck, J. Phys. A **19**, 211 (1986).

[40] R. Terras and R. Swanson, J. Math. Phys. **21**, 2140 (1980).

[41] R. Terras and R. A. Swanson, Am. J. Phys. **48**, 526 (1980).

[42] J. B. Keller, Communications on Pure and Applied Mathematics **6**, 505 (1953).

[43] J. Schwinger, L. L. DeRaad, Jr., K. A. Milton, and W.-y. Tsai, *Classical Electrodynamics* (Westview Press, New York, 1998).

[44] N. Inui, J. Phys. Soc. Jpn. **76**, 114002 (2007).

[45] H. Ahmedov and I. H. Duru, J. Math. Phys. **45**, 965 (2004).

[46] H. Ahmedov and I. H. Duru, J. Math. Phys. **46**, 022303 (2005).

[47] H. Ahmedov and I. H. Duru, Turk. J. Phys. **30**, 345 (2006).

[48] R. Terras, Math. Proc. Camb. Phil. Soc. **89**, 331 (1981).

[49] C. Kittel, *Introduction to Solid State Physics, 8th ed.* (Wiley, Hoboken, NJ, 2005).

[50] M. Born and K. Huang, *Dynamical Theory of Crystal Lattices* (Clarendon Press, New York, 1956).

[51] H. Kremer and E. W. Weisstein, From *MathWorld* – A Wolfram Web Resource. http://mathworld.wolfram.com/IsoperimetricQuotient.html .

[52] E. W. Weisstein, From *MathWorld* – A Wolfram Web Resource. http://mathworld.wolfram.com/IsoperimetricInequality.html .

[53] P. J. Nahin, *When least is best* (Princeton University Press, Princeton, NJ, 2004).

[54] M. G. Lamé, *Leçons sur la théorie mathématique de l'élasticité des corps solides* (Bachelier, Paris, 1852).

[55] B. J. McCartin, Mathematical Problems in Engineering **8**, 517 (2002).

[56] B. J. McCartin, SIAM Review **45**, 267 (2003).

[57] M. A. Pinsky, SIAM J. on Mathematical Analysis **11**, 819 (1979).

[58] M. Prager, Applications of Mathematics **43**, 311 (1998).

[59] P. Gosdzinsky and A. Romeo, Physics Letters B **441**, 265 (1998).

[60] K. A. Milton, A. V. Nesterenko, and V. V. Nesterenko, Phys. Rev. D **59**, 105009 (1999).

[61] I. Cavero-Peláez, K. A. Milton, and K. Kirsten, J. Phys. A **40**, 3607 (2007).

[62] J. W. Turner, J. Phys. A **17**, 2791 (1984).

[63] H. R. Krishnamurthy, H. S. Mani, and H. C. Verma, J. Phys. A **15**, 2131 (1982).

[64] C. M. Bender and K. A. Milton, Phys. Rev. D **50**, 6547 (1994).

[65] R. E. Crandall, http://people.reed.edu/ crandall/papers/epstein.pdf (1998).

[66] R. E. Crandall, Exp. Math. **8**, 367 (1999).

Appendix A

Poisson Resummation Formulæ

A.1 Discrete Mode Numbers

We consider the Poisson resummation of the traced cylinder kernel of an arbitrary real quadratic form,

$$\mathcal{S} = \sum_{m_1,\ldots,m_n=-\infty}^{\infty} e^{-\tau\sqrt{(m+a)_j\, A_{jk}\, (m+a)_k}}\,. \tag{A.1}$$

Taking the Fourier transform of the summand of $\mathcal{S}$ and using Eq. (3.2) gives

$$\mathcal{S} = \sum_{m_1,\ldots,m_n=-\infty}^{\infty} \int_{-\infty}^{\infty} \prod_{j=1}^{n} du_j\, e^{2\pi i u_j m_j} e^{-\tau\sqrt{(u_i+a_i)A_{ik}(u_k+a_k)}}\,. \tag{A.2}$$

We shift the variables

$$u_j \to u_j - a_j\,, \tag{A.3}$$

and diagonalize A

$$B_{ij} = U_{ik}\, A_{km}\, U^{\mathsf{T}}_{mj}\,. \tag{A.4}$$

A redefinition of the integration variables follows,

$$v_j = U_{jk} u_k\,, \tag{A.5}$$

as well as the summation variables,

$$q_j = U_{jk}\, m_k\,. \tag{A.6}$$

As a result of these transformations, we recognize that the Jacobian of the transformation matrix is unity,

$$\prod_{j=1}^{n} du_j = \prod_{j=1}^{n} dv_j\,. \tag{A.7}$$

We are now ready to change to hyperspherical coordinates. First, we define

$$R_j = \sqrt{B_{jj}}\, v_j \tag{A.8}$$

and

$$k_j = \frac{q_j}{\sqrt{B_{jj}}} \tag{A.9}$$

which allows us to write

$$v_j\, q_j = kR\cos\theta\,. \tag{A.10}$$

Effectuating the change of variables gives us

$$\prod_{j=1}^{n} dv_j = |\det(B)|^{-1/2}\, R^{n-1} dR\, d\phi\, (\sin\theta)^{n-2}\, d\theta \prod_{j=1}^{n-3} (\sin\theta_j)^j\; d\theta_j\,. \tag{A.11}$$

The ϕ-integral produces a 2π and the integrals for the first $(n-3)$ θ_j angles give

$$\prod_{j=1}^{n-3} \left(\int_0^{\pi} \sin^j\theta\, d\theta \right) = \frac{\pi^{(n-3)/2}}{\Gamma((n-1)/2)}\,. \tag{A.12}$$

We are now able to focus on the remaining θ-integral,

$$\int_0^{\pi} (\sin\theta)^{n-2}\, e^{2\pi i kR\cos\theta}\, d\theta = \pi^{(3-n)/2}\Gamma((n-1)/2)\,(kR)^{(2-n)/2}\, J_{(n-2)/2}(2\pi kR)\;. \tag{A.13}$$

The last integral, the R-integral, is evaluated rather straightforwardly,

$$\int_0^{\infty} dR\, R^{n/2} J_{(n-2)/2}(2\pi kR)\, e^{-\tau R} = \frac{\tau\, 2^{n-1}\pi^{(n-3)/2} k^{(n-2)/2}\Gamma\left((n-1)/2\right)}{\left(\tau^2 + 4\pi^2 k_j\, k_j\right)^{(n+1)/2}}\,, \tag{A.14}$$

and putting everything together we obtain:

$$\mathcal{S} = \frac{2^n \pi^{(n-1)/2}\,\Gamma((n+1)/2)}{|\det(A)|^{1/2}} \sum_{m_1,\ldots,m_n=-\infty}^{\infty} \frac{\tau\, e^{-2\pi i\, m_j\, a_j}}{\left(\tau^2 + 4\pi^2 k_j\, k_j\right)^{(n+1)/2}}\,. \tag{A.15}$$

A.2 Discrete and Continuous Mode Numbers

If $\mathcal{S}$, in Eq. (A.1), were to have discrete as well as continuous mode numbers,

$$\mathcal{S} = \int_{-\infty}^{\infty} \prod_{i=1}^{\alpha-1} dm_i \sum_{m_\alpha,\ldots,m_n=-\infty}^{\infty} e^{-\tau\sqrt{(m+a)_j\, A_{jk}\, (m+a)_k}}\,, \tag{A.16}$$

where the indices j, k run from 1 to n and $1 \leq \alpha \leq n$, we would simply obtain a slightly modified version of Eq. (A.15):

$$\mathcal{S} = \frac{2^n \pi^{(n-1)/2}\, \Gamma((n+1)/2)}{|\det(A)|^{1/2}} \sum_{m_\alpha,\ldots,m_n=-\infty}^{\infty} \frac{\tau\, e^{-2\pi i\, m_j\, a_j}}{(\tau^2 + 4\pi^2 k_j\, k_j)^{(n+1)/2}}\,. \tag{A.17}$$

The sum would now be only over the mode numbers $\{m_\alpha, \ldots, m_n\}$ and we would also have

$$m_j\, a_j = m_\alpha\, a_\alpha + \cdots + m_n\, a_n\,, \tag{A.18}$$

$$k_j\, k_j = k_\alpha\, k_\alpha + \cdots + k_n\, k_n\,, \tag{A.19}$$

with k_j defined in the previous section (A.9).

A.3 Continuous Mode Numbers

In particular, if we set $\alpha = n + 1$ in Eq. (A.16) or in other words the case where all mode numbers are continuous, S would become:

$$\mathcal{S} = \int_{-\infty}^{\infty} \prod_{i=1}^{n} dm_i\; e^{-\tau\sqrt{(m+a)_j\, A_{jk}\, (m+a)_k}}\,. \tag{A.20}$$

The result, after performing the integrals in hyperspherical coordinates would be of the simple form:

$$\mathcal{S} = \frac{2^n \pi^{(n-1)/2}\, \Gamma((n+1)/2)}{|\det(A)|^{1/2}\; \tau^n}\,. \tag{A.21}$$

Appendix B

Mathematical Functions

B.1 Epstein Zeta Functions

We define the following Epstein zeta functions:

$$Z_3(s;a,b,c) = \sum_{k,m,n=-\infty}^{\infty}{}' (a\,k^2 + b\,m^2 + c\,n^2)^{-s}, \tag{B.1}$$

$$Z_{3b}(s;a,b,c) = \sum_{k,m,n=-\infty}^{\infty}{}' (-1)^{k+m+n}(a\,k^2 + b\,m^2 + c\,n^2)^{-s}, \tag{B.2}$$

$$Z_{3c}(s;a,b,c) = \sum_{k,m,n=-\infty}^{\infty}{}' (-1)^{k+m}(a\,k^2 + b\,m^2 + c\,n^2)^{-s}, \tag{B.3}$$

$$Z_{2b}(s;a,b) = \sum_{m,n=-\infty}^{\infty}{}' (-1)^{m+n}(a\,m^2 + b\,n^2)^{-s}. \tag{B.4}$$

Here, sums are over all integers, positive, negative, and zero, excluding the single point where all are zero. They are summed numerically using Ewald's method [37, 65, 66]:

$$\begin{aligned} Z_3(s;a,b,c) =& \frac{1}{\Gamma(s)}\Bigg[-\frac{\alpha^s}{s} - \frac{\pi^{3/2}\alpha^{s-3/2}}{(3/2-s)} + \sum_{k,m,n=-\infty}^{\infty}{}' \frac{\Gamma(s;\alpha[ak^2+bm^2+cn^2])}{(ak^2+bm^2+cn^2)^s} \\ &+ \pi^{2s-3/2}\sum_{k,m,n=-\infty}^{\infty}{}' \frac{\Gamma(3/2-s;\pi^2/\alpha[k^2/a+m^2/b+n^2/c])}{(k^2/a+m^2/b+n^2/c)^{3/2-s}}\Bigg], \end{aligned} \tag{B.5}$$

$$\begin{aligned} Z_{3b}(s;a,b,c) =& \frac{1}{\Gamma(s)}\Bigg[-\frac{\alpha^s}{s} + \sum_{k,m,n=-\infty}^{\infty}{}' (-1)^{k+m+n}\frac{\Gamma(s;\alpha[ak^2+bm^2+cn^2])}{(ak^2+bm^2+cn^2)^s} \\ &+ \pi^{2s-3/2}\sum_{k,m,n=-\infty}^{\infty} \frac{\Gamma(3/2-s;\pi^2/\alpha|\mathbf{q}+\mathbf{c}|^2)}{|\mathbf{q}+\mathbf{c}|^{3-2s}}\Bigg], \end{aligned} \tag{B.6}$$

$$\begin{aligned} Z_{3c}(s;a,b,c) =& \frac{1}{\Gamma(s)}\Bigg[-\frac{\alpha^s}{s} + \sum_{k,m,n=-\infty}^{\infty}{}' (-1)^{k+m}\frac{\Gamma(s;\alpha[ak^2+bm^2+cn^2])}{(ak^2+bm^2+cn^2)^s} \\ &+ \pi^{2s-3/2}\sum_{k,m,n=-\infty}^{\infty} \frac{\Gamma(3/2-s;\pi^2/\alpha|\mathbf{q}+\mathbf{d}|^2)}{|\mathbf{q}+\mathbf{d}|^{3-2s}}\Bigg], \end{aligned} \tag{B.7}$$

$$Z_{2b}(s;a,b) = \frac{1}{\Gamma(s)}\Bigg[-\frac{\alpha^s}{s} + \sum_{m,n=-\infty}^{\infty}{}' (-1)^{m+n} \frac{\Gamma(s;\alpha[am^2+bn^2])}{(am^2+bn^2)^s} + \pi^{2s-1} \sum_{m,n=-\infty}^{\infty} \frac{\Gamma(1-s;\pi^2/\alpha[(m+1/2)^2/a+(n+1/2)^2/b])}{[(m+1/2)^2/a+(n+1/2)^2/b]^{1-s}} \Bigg], \tag{B.8}$$

where we have occasionally used the definitions $\mathbf{q} = (k/\sqrt{a}, m/\sqrt{b}, n/\sqrt{c})$, $\mathbf{c} = \frac{1}{2}(1/\sqrt{a}, 1/\sqrt{b}, 1/\sqrt{c})$, and $\mathbf{d} = \frac{1}{2}(1/\sqrt{a}, 1/\sqrt{b}, 0)$. The constant α is chosen such that $0 < \alpha < \infty$; for the sake of simplicity and computational efficiency it may be set $\alpha = 1$. A few specific Epstein zeta values needed for calculations:

$$Z_3(2;1,1,1) = 16.5323159598, \tag{B.9}$$

$$Z_{3b}(2;1,1,1) = -3.8631638072, \tag{B.10}$$

$$Z_{3c}(2;1,1,1) = -1.8973804658, \tag{B.11}$$

$$Z_{2b}(3/2;1,2) = -1.9367356117, \tag{B.12}$$

$$Z_{2b}(3/2;1,3) = -1.8390292892. \tag{B.13}$$

B.2 Dirichlet L-series

The Dirichlet L-series are defined as $L_k(s) = \sum_{n=1}^{\infty} \chi_k(n)\, n^{-s}$ where χ_k is the number-theoretic character [37]. The Dirichlet beta function, also known as L_{-4}, is usually defined as $\beta(s) = \sum_{n=0}^{\infty} (-1)^n (2n+1)^{-s}$.

B.3 Chowla-Selberg Formula

The Chowla-Selberg formula, for $\mathrm{Re}\, s > 1$ and $\Delta = 4ac - b^2 > 0$ is,

$$\sum_{m,n=-\infty}^{\infty}{}' (am^2 + bmn + cn^2)^{-s} = 2a^{-s}\zeta(2s) + \frac{2^{2s}\sqrt{\pi}a^{s-1}}{\Gamma(s)\Delta^{s-1/2}}\zeta(2s-1)\Gamma(s-1/2)$$
$$+ \frac{2^{s+5/2}\pi^s}{\Gamma(s)\Delta^{s/2-1/4}\sqrt{a}}\sum_{n=1}^{\infty} n^{s-1/2}\sigma_{1-2s}(n)\cos(n\pi b/a)K_{1/2-s}(n\pi\sqrt{\Delta}/a). \qquad \text{(B.14)}$$

The prime indicates $m = n = 0$ is excluded from the summation range. The divisor function, $\sigma_k(n)$, is the sum of the k-th powers of the divisors of n,

$$\sigma_k(n) \equiv \sum_{d|n} d^k. \qquad \text{(B.15)}$$